



HAL
open science

First observation of ^{28}O

Y Kondo, N.L Achouri, H. Al Falou, L Atar, T Aumann, H Baba, K Boretzky,
C Caesar, D Calvet, H Chae, et al.

► **To cite this version:**

Y Kondo, N.L Achouri, H. Al Falou, L Atar, T Aumann, et al.. First observation of ^{28}O . Nature, 2023, 620 (7976), pp.965-970. 10.1038/s41586-023-06352-6 . hal-04196834

HAL Id: hal-04196834

<https://hal.science/hal-04196834>

Submitted on 9 Oct 2023

HAL is a multi-disciplinary open access archive for the deposit and dissemination of scientific research documents, whether they are published or not. The documents may come from teaching and research institutions in France or abroad, or from public or private research centers.

L'archive ouverte pluridisciplinaire **HAL**, est destinée au dépôt et à la diffusion de documents scientifiques de niveau recherche, publiés ou non, émanant des établissements d'enseignement et de recherche français ou étrangers, des laboratoires publics ou privés.

1 First observation of ^{28}O

2 Y. Kondo*,¹ N.L. Achouri,² H. Al Falou,^{3,4} L. Atar,⁵ T. Aumann,^{5,6,7} H. Baba,⁸ K. Boretzky,⁶ C. Caesar,^{5,6} D. Calvet,⁹
3 H. Chae,¹⁰ N. Chiga,⁸ A. Corsi,⁹ F. Delaunay,² A. Delbart,⁹ Q. Deshayes,² Zs. Dombrádi,¹¹ C.A. Douma,¹² A. Ekström,¹³
4 Z. Elekes,¹¹ C. Forssén,¹³ I. Gašparić,^{14,8,5} J.-M. Gheller,⁹ J. Gibelin,² A. Gillibert,⁹ G. Hagen,^{15,16} M.N. Harakeh,^{6,12}
5 A. Hirayama,¹ C.R. Hoffman,¹⁷ M. Holl,^{5,6} A. Horvat,⁶ Á. Horváth,¹⁸ J.W. Hwang,^{19,20} T. Isobe,⁸ W.G. Jiang,¹³ J. Kahlbow,^{5,8}
6 N. Kalantar-Nayestanaki,¹² S. Kawase,²¹ S. Kim,^{19,20} K. Kisamori,⁸ T. Kobayashi,²² D. Körper,⁶ S. Koyama,²³ I. Kuti,¹¹
7 V. Lapoux,⁹ S. Lindberg,¹³ F.M. Marqués,² S. Masuoka,²⁴ J. Mayer,²⁵ K. Miki,²² T. Murakami,²⁶ M. Najafi,¹² T. Nakamura,¹
8 K. Nakano,²¹ N. Nakatsuka,²⁶ T. Nilsson,¹³ A. Obertelli,⁹ K. Ogata,^{27,28,29} F. de Oliveira Santos,³⁰ N.A. Orr,² H. Otsu,⁸
9 T. Otsuka,^{23,8} T. Ozaki,¹ V. Panin,⁸ T. Papenbrock,^{16,15} S. Paschalis,⁵ A. Revel,^{2,30} D. Rossi,⁵ A.T. Saito,¹ T.Y. Saito,²³
10 M. Sasano,⁸ H. Sato,⁸ Y. Satou,²⁰ H. Scheit,⁵ F. Schindler,⁵ P. Schrock,²⁴ M. Shikata,¹ N. Shimizu,³¹ Y. Shimizu,⁸ H. Simon,⁶
11 D. Sohler,¹¹ O. Sorlin,³⁰ L. Stuhl,^{19,8} Z.H. Sun,^{16,15} S. Takeuchi,¹ M. Tanaka,³² M. Thoennessen,³³ H. Törnqvist,^{6,5}
12 Y. Togano,^{34,1} T. Tomai,¹ J. Tscheuschner,⁵ J. Tsubota,¹ N. Tsunoda,²⁴ T. Uesaka,⁸ Y. Utsuno,³⁵ I. Vernon,³⁶ H. Wang,⁸
13 Z. Yang,⁸ M. Yasuda,¹ K. Yoneda,⁸ and S. Yoshida³⁷

14 ¹Department of Physics, Tokyo Institute of Technology, 2-12-1 O-Okayama, Meguro, Tokyo 152-8551, Japan. ²LPC Caen UMR6534, Université de Caen Normandie, ENSICAEN,
15 CNRS/IN2P3, F-14000 Caen, France. ³Lebanese University, Beirut, Lebanon. ⁴Lebanese-French University of Technology and Applied Science, Deddeh, Lebanon. ⁵Institut für
16 Kernphysik, Technische Universität Darmstadt, 64289 Darmstadt, Germany. ⁶GSI Helmholtzzentrum für Schwerionenforschung, 64291 Darmstadt, Germany. ⁷Helmholtz Research
17 Academy Hesse for FAIR, 64289 Darmstadt, Germany. ⁸RIKEN Nishina Center, Hirosawa 2-1, Wako, Saitama 351-0198, Japan. ⁹Irfu, CEA, Université Paris-Saclay, 91191
18 Gif-sur-Yvette, France. ¹⁰IBS, 55, expo-ro, yuseong-gu, Daejeon, 34126, Republic of Korea. ¹¹MTA Atomki, 4001 Debrecen, Hungary. ¹²ESRIG, University of Groningen,
19 Zernikelaan 25, 9747 AA Groningen, The Netherlands. ¹³Institutionen för Fysik, Chalmers Tekniska Högskola, 412 96 Göteborg, Sweden. ¹⁴Ruder Bošković Institute, Bijenička cesta
20 54, 10000 Zagreb, Croatia. ¹⁵Physics Division, Oak Ridge National Laboratory, Oak Ridge, Tennessee 37831, USA. ¹⁶Department of Physics and Astronomy, University of
21 Tennessee, Knoxville, TN 37996, USA. ¹⁷Physics Division, Argonne National Laboratory, Argonne, Illinois 60439, USA. ¹⁸Eötvös Loránd University, Pázmány Péter Sétány 1/A,
22 H-1117 Budapest, Hungary. ¹⁹Center for Exotic Nuclear Studies, Institute for Basic Science, Daejeon 34126, Republic of Korea. ²⁰Department of Physics and Astronomy, Seoul
23 National University, Gwanak-ro, Gwanak-gu, Seoul 08826, Republic of Korea. ²¹Department of Advanced Energy Engineering Science, Kyushu University, Kasuga, Fukuoka
24 819-0395, Japan. ²²Department of Physics, Tohoku University, Miyagi 980-8578, Japan. ²³University of Tokyo, Tokyo 1130033, Japan. ²⁴Center for Nuclear Study, University of
25 Tokyo, 2-1 Hirosawa, Wako, Saitama 351-0198, Japan. ²⁵Institut für Kernphysik, Universität zu Köln, 50937 Köln, Germany. ²⁶Department of Physics, Kyoto University, Kyoto
26 606-8502, Japan. ²⁷Department of Physics, Kyushu University, Fukuoka 819-0395, Japan. ²⁸Research Center for Nuclear Physics, Osaka University, Ibaraki, Japan. ²⁹Department of
27 Physics, Osaka City University, Osaka, Japan. ³⁰Grand Accélérateur National d'Ions Lourds (GANIL), CEA/DRF-CNRS/IN2P3, Bvd Henri Becquerel, 14076 Caen, France. ³¹Center
28 for Computational Sciences, University of Tsukuba, 1-1-1 Tennodai, Tsukuba 305-8577, Japan. ³²Department of Physics, Osaka University, Osaka 560-0043, Japan. ³³Facility for
29 Rare Isotope Beams, Michigan State University, East Lansing, Michigan 48824, USA. ³⁴Department of Physics, Rikkyo University, 3-34-1 Nishi-Ikebukuro, Toshima, Tokyo
30 172-8501, Japan. ³⁵Advanced Science Research Center, Japan Atomic Energy Agency, Tokai, Ibaraki 319-1195, Japan. ³⁶Department of Mathematical Sciences, Durham University,
31 Stockton Road, Durham, DH1 3LE, UK. ³⁷Liberal and General Education Center, Institute for Promotion of Higher Academic Education, Utsunomiya University, Tochigi, Japan.

Subjecting a physical system to extreme conditions is one of the means often employed to obtain a better understanding and deeper insight into its organization and structure. In the case of the atomic nucleus, one such approach is to investigate isotopes that have very different neutron-to-proton (N/Z) ratios than in stable nuclei. Light neutron-rich isotopes exhibit the most asymmetric N/Z ratios and those lying beyond the limits of binding, which undergo spontaneous neutron emission and exist only as very short-lived resonances ($\sim 10^{-21}$ seconds), provide the most stringent tests of modern nuclear structure theories. Here we report on the **first observation of ^{28}O and ^{27}O via their decay into ^{24}O and four and three neutrons. The ^{28}O nucleus is of particular interest as, with 8 protons and 20 neutrons, it is expected in the standard shell model picture of nuclear structure to be one of a relatively small number of so-called “doubly-magic” nuclei. Both ^{27}O and ^{28}O were found to exist as narrow low-lying resonances and their decay energies are compared here to the results of sophisticated theoretical modelling, including a large-scale shell model calculation and a newly developed statistical approach. In both cases, the underlying nuclear interactions were derived from effective field theories of quantum chromodynamics. Finally, it is shown that the cross section for the production of ^{28}O from a ^{29}F beam is consistent with it not exhibiting a closed $N = 20$ shell structure.**

32 One of the most active areas of present day nuclear physics
33 is the investigation of rare isotopes with large N/Z imbal-
34 ances. The structure of such nuclei provides for strong tests
35 of our theories, including most recently, sophisticated *ab initio*
36 type approaches whereby the underlying interactions between
37 the constituent nucleons are constructed from first principles
38 approaches (see, for example, ref.¹).

39 Owing to the strong nuclear force, nuclei remain bound to
40 the addition of many more neutrons than protons and the most
41 extremely N/Z asymmetries are found for light neutron-rich
42 nuclei (Fig. 1a). Here, beyond the limits of nuclear binding
43 — the so-called neutron dripline — nuclei can exist as very
44 short-lived ($\sim 10^{-21}$ seconds) resonances, which decay by
45 spontaneous neutron emission, with their energies and life-
46 times dependent on the underlying structure of the system.
47 Experimentally, such nuclei can only be reached for the light-
48 est systems (Fig. 1a), where the location of the neutron dripline

49 has been established up to neon ($Z = 10$)² and the heaviest
50 neutron unbound nucleus observed for fluorine ($Z = 9$) ^{28}F
51 (ref.³). **Arguably the most extreme system, if confirmed to**
52 **exist as a resonance, would be the tetra-neutron for which, a**
53 **narrow near threshold continuum structure has been found in**
54 **a recent missing mass measurement⁴.** Here we report on the
55 direct observation of ^{28}O ($N/Z = 2.5$), which is unbound to 4
56 neutron decay, and of neighbouring ^{27}O (3 neutron unbound).

57 The nucleus ^{28}O has long been of interest^{5,6} as, in the stan-
58 dard shell-model picture of nuclear structure, it is expected to
59 be “doubly magic”. **Indeed, it** is very well established that
60 for stable and near stable nuclei the proton and neutron num-
61 bers 2, 8, 20, 28, 50, 82, 126 correspond to spherical closed
62 shells^{7,8}. Such nuclei represent a cornerstone in our under-
63 standing of the structure of the many-body nuclear system. In
64 particular, as considerable energy is required to excite them
65 owing to the large shell gaps, they can be considered, when

66 modelling nuclei in their mass region, as an “inert” core with
67 no internal degrees of freedom. Such an approach has his-
68 torically enabled more tractable calculations to be made than
69 attempting to model an A -body ($A = Z + N$) nucleus from the
70 full ensemble of nucleons. Indeed, this approach has been a
71 fundamental premise of the shell model methods which have
72 enabled an extremely wide variety of structural properties of
73 nuclei to be described with good accuracy over a number of
74 decades (see e.g., ref.⁹).

75 Of the very limited number of nuclei that are expected to
76 be doubly magic based on the classical shell closures, ^{28}O is,
77 given its extreme N/Z asymmetry, the only one that is in prin-
78 ciple experimentally accessible that has yet to be observed. In
79 recent years, the doubly magic character of the two other such
80 neutron-rich nuclei, ^{78}Ni ($Z = 28, N = 50; N/Z = 1.8$)¹⁰ and
81 ^{132}Sn ($Z = 50, N = 82; N/Z = 1.6$)¹¹, has been confirmed.
82 The remaining candidate, two-neutron unbound nucleus ^{10}He
83 ($Z = 2, N = 8; N/Z = 4$), has been observed as a well-
84 defined resonance but its magicity or otherwise has yet to be
85 established (ref.¹²).

86 The $N = 20$ shell closure has long been known, however,
87 to disappear in the neutron-rich Ne, Na and Mg ($Z = 10$ –
88 12) isotopes (see, for example, refs.^{13,14}). This region is re-
89 ferred to as the “Island of Inversion” (IoI)¹⁵, whereby the en-
90 ergy gap between the neutron sd - and pf -shell orbitals, rather
91 than being well pronounced (Fig. 1b), is weakened or even
92 vanishes and configurations with neutrons excited into the
93 pf -shell orbitals dominate the ground state (gs) of these nu-
94 clei as shown schematically in Fig. 1c. The IoI nuclei with
95 such configurations are well deformed, rather than spheri-
96 cal, and exhibit low-lying excited states. Very recently, the
97 IoI has been shown to extend to the fluorine isotopes $^{28,29}\text{F}$
98 ($N = 19, 20$)^{3,16–18} which neighbour ^{28}O . On the other hand,
99 the last particle-bound oxygen isotope, ^{24}O has been found to
100 be doubly magic, with a new closed shell forming at $N = 16$
101 (refs.^{19–23}). As such, the structural character of the more
102 neutron-rich oxygen isotopes and, in particular, ^{28}O is an in-
103 triguing question. To date, however, only $^{25,26}\text{O}$ ($N = 17, 18$)
104 have been observed, as single- and two-neutron unbound sys-
105 tems respectively^{24–27}, with the latter existing as an extremely
106 narrow, barely unbound resonance.

107 The present investigation focussed on the search for $^{27,28}\text{O}$,
108 produced in high-energy reactions, through the direct detec-
109 tion of their decay products – ^{24}O and 3 or 4 neutrons. Critical
110 to the success of this work was the capability of the RIKEN
111 RIBF (RI Beam Factory) to produce intense neutron dripline
112 beams coupled to a thick active liquid hydrogen target system
113 and a high performance multi-neutron detection array.

114 Experiment

115 The neutron-unbound $^{27,28}\text{O}$ were produced via proton in-
116 duced nucleon knockout reactions from a 235 MeV per nu-
117 cleon beam of ^{29}F . As depicted in Extended Data Fig. 1 the
118 ^{29}F ions were characterised and tracked onto a thick (151 mm)
119 liquid hydrogen reaction target using plastic scintillators and
120 multi-wire drift chambers (MWDCs). The hydrogen target
121 was surrounded by a time projection chamber (MINOS²⁸)
122 which allowed for the determination of the reaction vertex.
123 This combination provided for both the maximum possible
124 luminosity together with the ability to maintain a good $^{27,28}\text{O}$
125 decay energy resolution.

126 The forward focussed beam velocity reaction products –

127 charged fragments and fast neutrons – were detected and their
128 momenta determined, using the SAMURAI spectrometer²⁹
129 including the three large-area segmented plastic scintillator
130 walls of the NeuLAND³⁰ and NEBULA arrays. An overall
131 detection efficiency for the 3 and 4 neutron decay of around
132 2 and 0.4% was achieved for decay energies of ~ 0.5 MeV
133 (Extended Data Fig. 1). The decay energies were recon-
134 structed from the measured momenta using the invariant-mass
135 technique with a resolution (FWHM) of around 0.2 MeV at
136 ~ 0.5 MeV decay energy (see Methods).

137 Analysis and results

138 The ^{24}O fragments were identified by the magnetic rigid-
139 ity, energy loss and time-of-flight derived from the SAMU-
140 RAI spectrometer detectors. The neutrons incident on the
141 NeuLAND and NEBULA arrays were identified based on the
142 time-of-flight and energy deposited in the plastic scintillators.
143 Importantly, the multi-neutron detection required the applica-
144 tion of dedicated off-line analysis procedures in order to reject
145 crosstalk (see Methods) – that is, events in which a neutron is
146 scattered between and registered in two or more scintillators.

147 In the analysis, the decay neutrons were denoted $n_1, n_2,$
148 \dots by ascending order of the two-body relative energy E_{0i}
149 between ^{24}O and n_i – such that $E_{01} < E_{02} < E_{03} < E_{04}$
150 (Fig. 2d). The ^{28}O decay energy, E_{01234} , reconstructed from
151 the measured momentum vectors of the five decay particles,
152 is shown in Fig. 2a. A narrow peak is clearly observed at
153 ~ 0.5 MeV and may be assigned to be the ^{28}O ground state.
154 As a small fraction of crosstalk events could not be elimi-
155 nated by the rejection procedures care must be taken to under-
156 stand their contribution to the E_{01234} spectrum. In particular,
157 $^{24}\text{O}+3n$ events, in which one of the neutrons creates crosstalk
158 and is not identified as such in the analysis can mimic true
159 ^{28}O decay. In this context, in order to provide a complete and
160 consistent description of all the $^{24}\text{O}+xn$ decay energy spec-
161 tra, a full Monte-Carlo simulation was constructed (see Meth-
162 ods). As shown in Fig. 2a the contribution from the residual
163 cross talk events is found to be rather limited in magnitude in
164 the $^{24}\text{O}+4n$ decay energy spectrum and, moreover, produces
165 a very broad distribution .

166 The decay of ^{28}O was investigated by examining the corre-
167 lations in the ^{24}O plus neutrons subsystems (see Methods). In
168 particular, the three-body ($^{24}\text{O}+n_1+n_2$) partial decay energy
169 E_{012} (Extended Data Fig. 2a) was reconstructed from the ^{24}O
170 + $4n$ data set. The corresponding spectrum exhibits a sharp
171 threshold peak arising from $^{26}\text{O}_{\text{gs}}$, which is known to have
172 a decay energy of only 18(5) keV²⁷. This observation clearly
173 indicates that ^{28}O sequentially decays through $^{26}\text{O}_{\text{gs}}$ as shown
174 by the arrows A and B in Fig. 2e.

175 We have also observed, in the $^{24}\text{O}+3n$ channel, a ^{27}O reso-
176 nance for the first time, as may be seen in the four-body decay
177 energy (E_{0123}) spectrum of Fig. 2b. As confirmed by the simu-
178 lations, which are able to simultaneously describe the $^{24}\text{O}+3n$
179 and $4n$ decay energy spectra, the well populated peak-like
180 structure below ~ 0.5 MeV corresponds to ^{28}O events where
181 only three of the four emitted neutrons are detected. The
182 peak at $E_{0123} \sim 1$ MeV, however, cannot be generated by such
183 events and must arise from a ^{27}O resonance. This was con-
184 firmed by the analysis of the data acquired with a ^{29}Ne beam
185 (see Methods and Extended Data Fig. 2e) where ^{27}O can be
186 produced by two-proton removal but not ^{28}O as this requires
187 the addition of a neutron. The ^{27}O resonance also decays se-

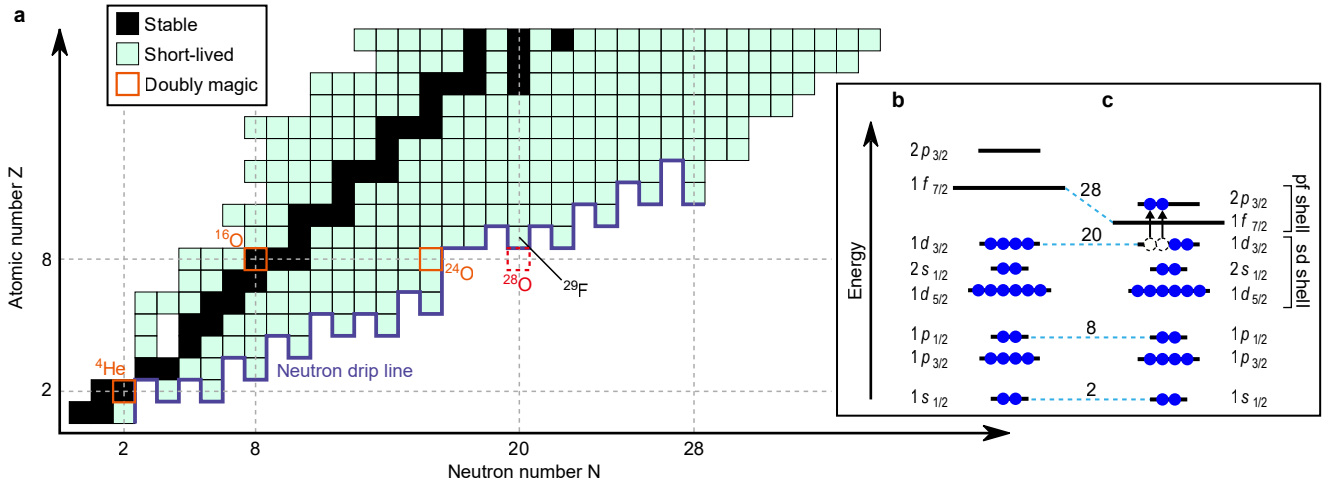


Fig. 1 | Nuclear chart and shell structure. **a)** Nuclear chart up to $Z = 18$ showing the stable and short-lived (β -decaying) nuclei. The experimentally established neutron dripline is shown by the thick blue line. Known doubly-magic nuclei are also indicated. **b)** Schematic illustration of the neutron configuration for a nucleus with a closed $N = 20$ shell. **c)** The neutron configuration involving particle-hole excitations across a quenched $N = 20$ shell gap.

188 sequentially via $^{26}\text{O}_{\text{gs}}$ as shown by the arrows B and C in Fig. 2e
 189 from the analysis of the partial decay energies (Extended Data
 190 Figs.2c and d).

191 The decay energies of the $^{27,28}\text{O}$ resonances were derived
 192 from a fit of the E_{0123} spectrum with the condition that the par-
 193 tial decay energy satisfies $E_{012} < 0.08$ MeV (Fig. 2c) – that
 194 is, decay via the ^{26}O ground-state was selected so as to mini-
 195 mize the uncertainties due to contributions from higher lying
 196 ^{28}O resonances which were not identified in the present mea-
 197 surements owing to the limited detection efficiency (Extended
 198 Data Fig. 1). The fitting employed lineshapes which incor-
 199 porated the effects of the experimental response functions, as
 200 derived from the simulations, including the contribution aris-
 201 ing from the residual crosstalk (see Methods).

202 In the case of ^{28}O a decay energy of
 203 $E_{01234} = 0.46^{+0.05}_{-0.04}(\text{stat}) \pm 0.02(\text{syst})$ MeV was found with
 204 an upper limit of the width of the resonance of 0.7 MeV (68%
 205 confidence interval). The cross section for single-proton
 206 removal from ^{29}F populating the resonance was deduced to be
 207 $1.36^{+0.16}_{-0.14}(\text{stat}) \pm 0.13(\text{syst})$ mb. The systematic uncertainties
 208 for the decay energy and the width were dominated by the
 209 precise conditions employed in the neutron crosstalk rejection
 210 procedures, while the principal contribution to that for the
 211 cross section arose from the uncertainty in the neutron detec-
 212 tion efficiency. It may be noted that if the resonance observed
 213 here is an excited state of ^{28}O (presumably the 2^+ level), then
 214 the ground state must lie even closer to threshold and the
 215 excitation energy of the former must be less than 0.46 MeV.
 216 This, however, is very much lower than theory suggests
 217 (2 MeV or more), even when the $N = 20$ shell-closure is
 218 absent (see below). As such, it is concluded that the ground
 219 state has been observed.

220 In the case of ^{27}O a decay energy of
 221 $E_{0123} = 1.09 \pm 0.04(\text{stat}) \pm 0.02(\text{syst})$ MeV was found. The
 222 width of the resonance was comparable to the estimated
 223 experimental resolution of 0.22 MeV (FWHM). Nevertheless,
 224 it was possible to obtain an upper limit on the width –
 225 0.18 MeV (68% confidence interval) – through a fit of a
 226 gated E_{012} spectrum for the much higher statistics ^{24}O and

227 two-neutron coincidence events, as shown in Extended Data
 228 Fig. 2f. The spin and parity (J^π) of the resonance may be
 229 tentatively assigned to be $3/2^+$ or $7/2^-$ based on the upper
 230 limit of the width (see Methods).

231 Comparison to theory

232 The experimental ground-state energies of the oxygen iso-
 233 topes $^{25-28}\text{O}$ are summarized in Fig. 3 and compared to
 234 theoretical calculations based on chiral effective field theory
 235 (χ EFT)^{32,33,37–40} and large-scale shell model calculations^{9,34}
 236 including those with continuum effects^{35,36}. We focus
 237 on large-scale shell-model and coupled-cluster calculations,
 238 where the latter is augmented with a novel statistical method.
 239 Both techniques include explicitly three-nucleon forces which
 240 are known to play a key role in describing the structure of
 241 neutron-rich nuclei, including the oxygen isotopes and the lo-
 242 cation of the $Z = 8$ neutron dripline at ^{24}O (refs.^{41–43}).

243 The large-scale shell model calculations were undertaken
 244 using the new EEdf3 interaction which was constructed based
 245 on χ EFT (see Methods). Since the calculations employ a
 246 model space which includes the pf shell orbitals, the dis-
 247 appearance of the $N = 20$ shell closure can be naturally
 248 described. The EEdf3 interaction is a modified version of
 249 EEdf1^{32,33}, which predicts correctly the neutron dripline at F,
 250 Ne and Na, as well as a relatively low-lying ^{29}F excited state¹⁷
 251 and the appreciable occupancy of the neutron $2p_{3/2}$ orbital^{3,18}.
 252 The EEdf3 interaction, which includes the effects of the EFT
 253 three-nucleon forces⁴⁴, provides a reasonable description of
 254 the trends in the masses of the oxygen isotopes. However, as
 255 may be seen in Fig. 3 it predicts somewhat higher $^{27,28}\text{O}$ ener-
 256 gies (~ 1 MeV) than found in the experiment. The calculated
 257 sum of the occupation numbers for the neutron pf -shell or-
 258 bitals is 2.5 (1.4) for ^{28}O (^{27}O) and for the $1d_{3/2}$ orbital 2.0
 259 (2.1), which are consistent with a collapse of the $N = 20$ shell
 260 closure. The EEdf3 calculations show that $^{28}\text{O}_{\text{gs}}$ has large
 261 admixtures of configurations involving neutron excitations in
 262 the pf -shell orbitals as expected for nuclei in the IoI. This is
 263 supported by the measured cross section as discussed below.

264 First-principle calculations were performed using the

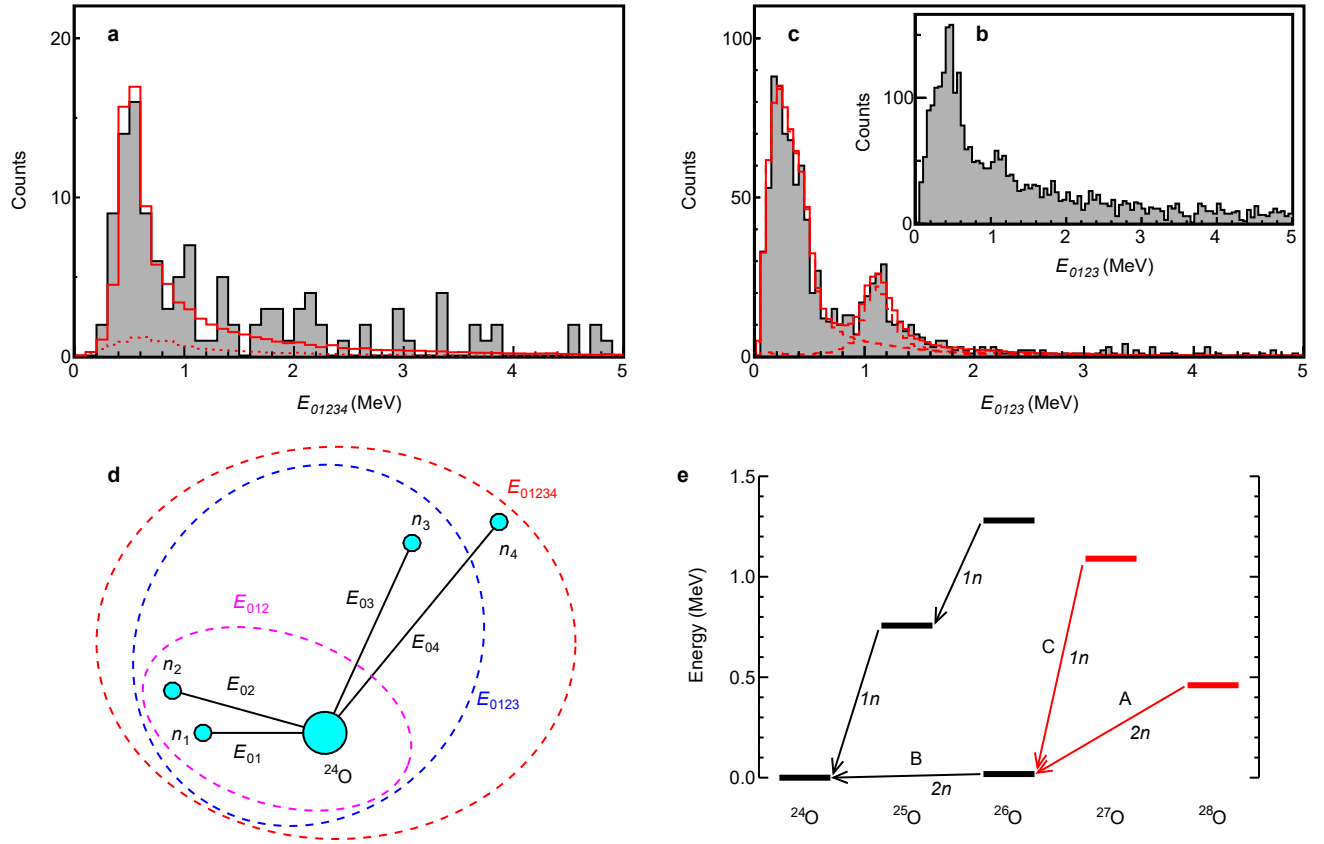


Fig. 2 | Decay energy spectra and decay scheme. **a)** Five-body decay energy (E_{01234}) spectrum for $^{24}\text{O}+4n$ events. The red-solid histogram shows the best-fit result taking into account the experimental response function. The dotted histogram shows the contribution arising from residual crosstalk that survives the rejection procedures (see Methods). **b)** Four-body decay energy (E_{0123}) spectrum for $^{24}\text{O}+3n$ events. **c)** Same as b, but gated by the partial decay energy $E_{012} < 0.08$ MeV. The red-dashed histograms represent the contributions from ^{28}O and ^{27}O events, and the red-solid histogram shows the sum. **d)** Definition of the partial decay energies. **e)** Decay scheme of the unbound oxygen isotopes. The newly observed resonances and their decays are shown in red.

265 coupled-cluster (CC) method guided by history matching
 266 (HM)^{45–47} to explore the parameter space of the 17 low-
 267 energy constants (LECs) in the χ EFT description of the two-
 268 and three-nucleon interactions. HM identifies the region of
 269 parameter space for which the emulated CC method generates
 270 non-implausible results (see Methods). A reliable low-
 271 statistic sample of 121 different LEC parameterizations was
 272 extracted for which the CC posterior predictive distribution
 273 (ppd) was computed for the ground-state energies of $^{27,28}\text{O}$,
 274 which are shown in Fig. 3. The predicted $^{27,28}\text{O}$ energies are
 275 correlated, as is clearly seen in the plot of energy distributions
 276 displayed in Extended Data Fig. 3. From this, the median values
 277 and 68% credible regions were obtained for the ^{27}O – ^{28}O
 278 and ^{28}O – ^{24}O energy differences: $\Delta E(^{27,28}\text{O})=0.11_{-0.39}^{+0.05}$ MeV
 279 and $\Delta E(^{28,24}\text{O})=2.1_{+1.2}^{-1.3}$ MeV. The experimental values
 280 $\Delta E(^{27,28}\text{O})=0.63\pm 0.06(\text{stat})\pm 0.03(\text{syst})$ MeV and
 281 $\Delta E(^{28,24}\text{O})=0.46_{-0.04}^{+0.05}(\text{stat})\pm 0.02(\text{syst})$ MeV, located at the
 282 edge of the 68% credible region, are consistent with the CC
 283 ppd. However, it is far enough away from the maximum to
 284 suggest that only a few finely-tuned chiral interactions may be
 285 able to reproduce the ^{27}O and ^{28}O energies. In addition, the
 286 obtained credible regions of the $^{27,28}\text{O}$ energies with respect
 287 to ^{24}O are relatively large, demonstrating that the measured
 288 decay energies of the extremely neutron-rich isotopes $^{27,28}\text{O}$

289 are valuable anchors for theoretical approaches based on
 290 χ EFT.

291 In Fig. 3 the predictions of a range of other models are dis-
 292 played. The USDB⁹ effective interaction (constructed within
 293 the sd shell) provides for arguably the most reliable predic-
 294 tions of the properties of sd -shell nuclei. The continuum shell
 295 model (CSM)³⁵ and the Gamow shell model (GSM)³⁶ include
 296 the effects of the continuum, which should be important for
 297 dripline and unbound nuclei. The shell-model calculation em-
 298 ploying the SDPF-M interaction³⁴ includes the pf shell or-
 299 bitals in its model space, which should be important if either
 300 or both $^{27,28}\text{O}$ lie within the IoI. All the calculations, except
 301 those with the SDPF-M interaction, predict a $J^\pi = 3/2^+ ^{27}\text{O}_{\text{gs}}$.
 302 In the case of the SDPF-M, a $3/2^-$ ground state is found with
 303 essentially degenerate $3/2^+$ (energy plotted in Fig. 3) and $7/2^-$
 304 excited states at 0.71 MeV.

305 The remaining theoretical predictions are based on χ EFT
 306 interactions. The valence-space in-medium similarity renor-
 307 malization group (VS-IMSRG)³⁷ employs the 1.8/2.0 (EM)
 308 EFT potential⁴⁴. The results for the self-consistent Green’s
 309 function (SCGF) approach are shown for the NNLO_{sat}⁴⁸ and
 310 NN+3N(Inl) potentials³⁸. The coupled-cluster calculation (Λ -
 311 CCSD(T)³⁹) using NNLO_{sat} is also shown. Except for the re-
 312 sults obtained using the GSM, all of the calculations shown
 313 predict higher energies than found here for ^{27}O and ^{28}O .

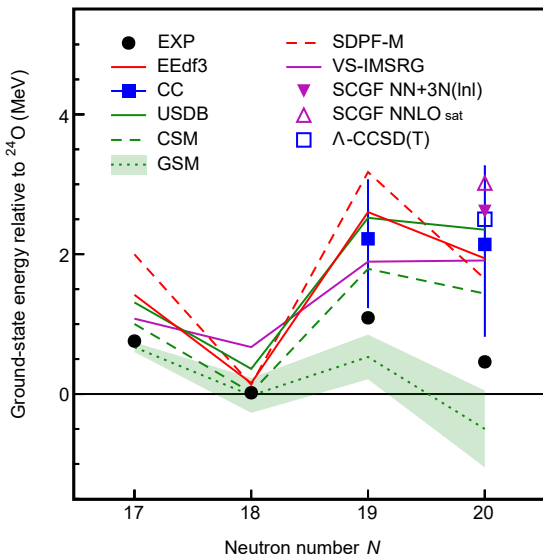


Fig. 3 | Ground-state energies with respect to ^{24}O . Experiment is shown by the filled circles where the values for $^{27,28}\text{O}$ are the present results and those for $^{25,26}\text{O}$ are taken from the atomic mass evaluation³¹. The experimental uncertainties are smaller than the symbol size. Comparison is made with predictions of shell-model calculations employing the EEdf3^{32,33}, USDB⁹ and SDPF-M³⁴ (see text for ^{27}O) interactions, the coupled-cluster method with the statistical approach (CC) and shell-model calculations incorporating continuum effects (CSM³⁵ and GSM³⁶). Also shown are the predictions of *ab initio* approaches (VS-IMSRG³⁷, SCGF³⁸, and Λ -CCSD(T)³⁹). The vertical bars for CC denote 68% credible intervals. The shaded band for GSM shows the uncertainties owing to *pf*-continuum couplings.

We now turn to the question of whether the $N = 20$ shell closure occurs in ^{28}O . Specifically, the measured cross section for single-proton removal from ^{29}F may be used to deduce the corresponding spectroscopic factor (C^2S) – a measure of the degree of overlap between initial and final state wave functions. As noted in the Introduction, the $N = 20$ shell closure disappears in ^{29}F and the ground state is dominated by neutron *pf*-shell configurations^{3,16–18}. As such, if the neutron configuration of ^{28}O is very similar to ^{29}F and the $Z = 8$ shell closure is rigid, the spectroscopic factor for proton removal will be close to unity. The spectroscopic factor was deduced using the distorted-wave impulse approximation (DWIA) approach (see Methods). As recent theoretical calculations predict $J^\pi = 5/2^+$ or $1/2^+$ for $^{29}\text{F}_{\text{gs}}$ (see, for example, refs.^{3,32,33,49–51}), the momentum distribution has been investigated (Extended Data Fig. 4) and was found to be consistent with proton removal from the $1d_{5/2}$ orbital (see Methods), leading to a $5/2^+$ assignment. The ratio of the measured to theoretical single-particle cross section provides for an experimentally deduced spectroscopic factor of $C^2S = 0.48_{-0.06}^{+0.05}(\text{stat}) \pm 0.05(\text{syst})$. Such an appreciable strength indicates that the ^{28}O neutron configuration resembles quite strongly that of ^{29}F . This value may be compared to that of 0.68 derived from the EEdf3 shell model calculations (where the center-of-mass correction factor⁵² $(29/28)^2$ has been applied). The 30% difference between the experimental C^2S as compared to theory, is in line with the well-known

reduction factor observed in (*p*, *2p*) and (*e*, *e'p*) reactions⁵³. Importantly, the EEdf3 calculations predict admixtures of the ground state wave function of ^{29}F with *sd*-closed-shell configurations of only some 12%. Consequently, even when the neutrons in ^{28}O are confined to the *sd* shell a spectroscopic factor of only 0.13 is obtained. As such, it is concluded that, as in ^{29}F , the *pf*-shell neutron configurations play a major role in ^{28}O and that the $N = 20$ shell closure disappears. Consequently the IoI extends to ^{28}O and it is not a doubly-magic nucleus.

More effort will be required to properly quantify the character of the structure of ^{28}O and the neutron *pf*-shell configurations. In this context, the determination of excitation energy of the first 2^+ state is the next step which may be envisaged experimentally¹⁷. The EEdf3 calculations predict an excitation energy of 2.097 MeV, which is close to that of ~ 2.5 MeV computed by the particle rotor model assuming moderate deformation⁵⁴. Both predictions are much lower than the energies found in doubly-magic nuclei – e.g., 6.917 MeV in ^{16}O and 4.7 MeV in ^{24}O (refs.^{21,23}). A complementary probe of the neutron *sd* – *pf*-shell gap, which is within experimental reach, is the energy difference between the positive- and negative-parity states of ^{27}O as seen in ^{28}F (ref.³).

Conclusions

We have reported here on the first observation of the extremely neutron-rich oxygen isotopes $^{27,28}\text{O}$. Both nuclei were found to exist as relatively low-lying resonances. These observations were made possible using a state-of-the-art setup which permitted the direct detection of 3 and 4 neutrons. From an experimental point of view, the multi-neutron-decay spectroscopy demonstrated here opens up new perspectives in the investigation of other extremely neutron-rich systems lying beyond the neutron dripline and the study of multi-neutron correlations. Comparison of the measured energies of $^{27,28}\text{O}$ with respect to ^{24}O with a broad range of theoretical predictions, including two approaches employing nuclear interactions derived from effective field theories of quantum chromodynamics, showed that in almost all cases theory underbinds both systems. The statistical coupled-cluster calculations indicated that the energies of $^{27,28}\text{O}$ can provide valuable constraints of such *ab initio* approaches and, in particular, the interactions employed. Finally, while ^{28}O is expected in the standard shell-model picture to be a doubly-magic nucleus ($Z = 8$ and $N = 20$), the single-proton removal cross section measured here, when compared to theory, was found to be consistent with it not having a closed neutron shell character. This result suggests that the island of inversion extends beyond $^{28,29}\text{F}$ into the oxygen isotopes.

- Hergert, H. A Guided Tour of *ab initio* Nuclear Many-Body Theory. *Front. Phys.* **8**, (2020).
- Ahn, D. S. *et al.* Location of the Neutron Dripline at Fluorine and Neon. *Phys. Rev. Lett.* **123**, 212501 (2019).
- Revel, A. *et al.* Extending the Southern Shore of the Island of Inversion to ^{28}F . *Phys. Rev. Lett.* **124**, 152502 (2020).
- Duer, M. *et al.* Observation of a correlated free four-neutron system. *Nature* **606**, 678–682 (2022).
- Sakurai, H. *et al.* Evidence for particle stability of ^{31}F and particle instability of ^{25}N and ^{28}O . *Phys. Lett. B* **448**, 180–184 (1999).

6. Tarasov, O. *et al.* Search for ^{28}O and study of neutron-rich nuclei near the $N = 20$ shell closure. *Phys. Lett. B* **409**, 64–70 (1997).
7. Mayer, M. G. On Closed Shells in Nuclei. II. *Phys. Rev.* **75**, 1969–1970 (1949).
8. Haxel, O., Jensen, J. H. D. & Suess, H. E. On the "Magic Numbers" in Nuclear Structure. *Phys. Rev.* **75**, 1766–1766 (1949).
9. Brown, B. A. & Richter, W. A. New "USD" Hamiltonians for the sd shell. *Phys. Rev. C* **74**, 034315 (2006).
10. Taniuchi, R. *et al.* ^{78}Ni revealed as a doubly magic stronghold against nuclear deformation. *Nature* **569**, 53–58 (2019).
11. Jones, K. L. *et al.* The magic nature of ^{132}Sn explored through the single-particle states of ^{133}Sn . *Nature* **465**, 454–457 (2010).
12. Matta, A. *et al.* New findings on structure and production of ^{10}He from ^{11}Li with the $(d, ^3\text{He})$ reaction. *Phys. Rev. C* **92**, 041302(R) (2015). and references therein.
13. Orr, N. A. *et al.* New mass measurements of neutron-rich nuclei near $N=20$. *Phys. Lett. B* **258**, 29–34 (1991).
14. Otsuka, T., Gade, A., Sorlin, O., Suzuki, T. & Utsuno, Y. Evolution of shell structure in exotic nuclei. *Rev. Mod. Phys.* **92**, 015002 (2020).
15. Warburton, E. K., Becker, J. A. & Brown, B. A. Mass systematics for $A=29$ –44 nuclei: The deformed $A\sim 32$ region. *Phys. Rev. C* **41**, 1147–1166 (1990).
16. Gaodefroy, L. *et al.* Direct Mass Measurements of ^{19}B , ^{22}C , ^{29}F , ^{31}Ne , ^{34}Na and Other Light Exotic Nuclei. *Phys. Rev. Lett.* **109**, 202503 (2012).
17. Doornenbal, P. *et al.* Low- Z shore of the "island of inversion" and the reduced neutron magicity toward ^{28}O . *Phys. Rev. C* **95**, 041301 (2017).
18. Bagchi, S. *et al.* Two-Neutron Halo is Unveiled in ^{29}F . *Phys. Rev. Lett.* **124**, 222504 (2020).
19. Ozawa, A., Kobayashi, T., Suzuki, T., Yoshida, K. & Tanihata, I. New Magic Number, $N = 16$, near the Neutron Drip Line. *Phys. Rev. Lett.* **84**, 5493–5495 (2000).
20. Otsuka, T. *et al.* Magic Numbers in Exotic Nuclei and Spin-Isospin Properties of the NN Interaction. *Phys. Rev. Lett.* **87**, 082502 (2001).
21. Hoffman, C. R. *et al.* Evidence for a doubly magic ^{24}O . *Phys. Lett. B* **672**, 17–21 (2009).
22. Kanungo, R. *et al.* One-Neutron Removal Measurement Reveals ^{24}O as a New Doubly Magic Nucleus. *Phys. Rev. Lett.* **102**, 152501 (2009).
23. Tshoo, K. *et al.* $N = 16$ Spherical Shell Closure in ^{24}O . *Phys. Rev. Lett.* **109**, 022501 (2012).
24. Hoffman, C. R. *et al.* Determination of the $N = 16$ Shell Closure at the Oxygen Drip Line. *Phys. Rev. Lett.* **100**, 152502 (2008).
25. Lunderberg, E. *et al.* Evidence for the Ground-State Resonance of ^{26}O . *Phys. Rev. Lett.* **108**, 142503 (2012).
26. Caesar, C. *et al.* Beyond the neutron drip line: The unbound oxygen isotopes ^{25}O and ^{26}O . *Phys. Rev. C* **88**, 034313 (2013).
27. Kondo, Y. *et al.* Nucleus ^{26}O : A Barely Unbound System beyond the Drip Line. *Phys. Rev. Lett.* **116**, 102503 (2016).
28. Obertelli, A. *et al.* MINOS: A vertex tracker coupled to a thick liquid-hydrogen target for in-beam spectroscopy of exotic nuclei. *Eur. Phys. J. A* **50**, 8 (2014).
29. Kobayashi, T. *et al.* SAMURAI spectrometer for RI beam experiments. *Nucl. Instrum. Methods Phys. Res., Sect. B* **317**, 294–304 (2013).
30. Boretzky, K. *et al.* NeuLAND: The high-resolution neutron time-of-flight spectrometer for R3B at FAIR. *Nucl. Instrum. Methods Phys. Res., Sect. A* **1014**, 165701 (2021).
31. Wang, M., Huang, W., Kondev, F., Audi, G. & Naimi, S. The AME 2020 atomic mass evaluation (II). Tables, graphs and references. *Chinese Physics C* **45**, 030003 (2021).
32. Tsunoda, N. *et al.* Exotic neutron-rich medium-mass nuclei with realistic nuclear forces. *Phys. Rev. C* **95**, 021304 (2017).
33. Tsunoda, N. *et al.* The impact of nuclear shape on the emergence of the neutron dripline. *Nature* **587**, 66–71 (2020).
34. Utsuno, Y., Otsuka, T., Mizusaki, T. & Honma, M. Varying shell gap and deformation in $N \sim 20$ unstable nuclei studied by the Monte Carlo shell model. *Phys. Rev. C* **60**, 054315 (1999).
35. Volya, A. & Zelevinsky, V. Continuum shell model. *Phys. Rev. C* **74**, 064314 (2006).
36. Fossez, K., Rotureau, J., Michel, N. & Nazarewicz, W. Continuum effects in neutron-drip-line oxygen isotopes. *Phys. Rev. C* **96**, 024308 (2017).
37. Stroberg, S. R., Holt, J. D., Schwenk, A. & Simonis, J. Ab Initio Limits of Atomic Nuclei. *Phys. Rev. Lett.* **126**, 022501 (2021).
38. Somà, V., Navrátil, P., Raimondi, F., Barbieri, C. & Duguet, T. Novel chiral Hamiltonian and observables in light and medium-mass nuclei. *Phys. Rev. C* **101**, 014318 (2020).
39. Hagen, G., Hjorth-Jensen, M., Jansen, G. R. & Papenbrock, T. Emergent properties of nuclei from ab initio coupled-cluster calculations. *Phys. Scr.* **91**, (2016).
40. Bogner, S. K. *et al.* Nonperturbative Shell-Model Interactions from the In-Medium Similarity Renormalization Group. *Phys. Rev. Lett.* **113**, 142501 (2014).
41. Otsuka, T., Suzuki, T., Holt, J. D., Schwenk, A. & Akaishi, Y. Three-Body Forces and the Limit of Oxygen Isotopes. *Phys. Rev. Lett.* **105**, 032501 (2010).
42. Hagen, G., Hjorth-Jensen, M., Jansen, G. R., Machleidt, R. & Papenbrock, T. Continuum Effects and Three-Nucleon Forces in Neutron-Rich Oxygen Isotopes. *Phys. Rev. Lett.* **108**, 242501 (2012).
43. Holt, J., Menéndez, J. & Schwenk, A. Chiral three-nucleon forces and bound excited states in neutron-rich oxygen isotopes. *Eur. Phys. J. A* **49**, (2013).
44. Hebeler, K., Bogner, S. K., Furnstahl, R. J., Nogga, A. & Schwenk, A. Improved nuclear matter calculations from chiral low-momentum interactions. *Phys. Rev. C* **83**, 031301 (2011).
45. Vernon, I., Goldstein, M. & Bower, R. G. Galaxy formation: a Bayesian uncertainty analysis. *Bayesian Anal.* **5**, 619–669 (2010).
46. Vernon, I., Goldstein, M. & Bower, R. Galaxy Formation: Bayesian History Matching for the Observable Universe. *Statist. Sci.* **29**, 81–90 (2014).
47. Vernon, I. *et al.* Bayesian uncertainty analysis for complex systems biology models: emulation, global parameter searches and evaluation of gene functions. *BMC Systems Biology* **12**, 1 (2018).
48. Ekström, A. *et al.* Accurate nuclear radii and binding energies from a chiral interaction. *Phys. Rev. C* **91**, 051301 (2015).
49. Utsuno, Y. *et al.* Shape transitions in exotic Si and S isotopes and tensor-force-driven Jahn-Teller effect. *Phys. Rev. C* **86**, 051301(R) (2012).
50. Caurier, E., Nowacki, F. & Poves, A. Merging of the islands of inversion at $N = 20$ and $N = 28$. *Phys. Rev. C* **90**, 014302 (2014).
51. Fossez, K. & Rotureau, J. Density matrix renormalization group description of the island of inversion isotopes $^{28-33}\text{F}$. *Phys. Rev. C* **106**, 034312 (2022).
52. Dieperink, A. E. L. & de Forest, T. Center-of-mass effects in single-nucleon knock-out reactions. *Phys. Rev. C* **10**, 543–549 (1974).
53. Wakasa, T., Ogata, K. & Noro, T. Proton-induced knockout reactions with polarized and unpolarized beams. *Prog. Part. Nucl. Phys.* **96**, 32–87 (2017).
54. Macchiavelli, A. *et al.* Structure of ^{29}F in the rotation-aligned coupling scheme of the particle-rotor model. *Phys. Lett. B* **775**, 160–162 (2017).

METHODS

Production of the ^{29}F beam The beam of ^{29}F ions was provided by the RI Beam Factory operated by the RIKEN Nishina Center and the Center for Nuclear Study (CNS), University of Tokyo. It was produced by projectile fragmentation of an intense 345 MeV per nucleon ^{48}Ca beam on a 15-mm-thick beryllium target. The secondary beam, including ^{29}F , was prepared using the BigRIPS⁵⁵ fragment separator operated with aluminum degraders of 15-mm and 7-mm median thicknesses at the first and fifth intermediate focal planes, respectively. The primary ^{48}Ca beam intensity was typically 3×10^{12} particles per second. The average intensity of the ^{29}F beam was 90 particles per second.

Measurement with a ^{29}Ne beam Data was also acquired to measure the direct population of ^{27}O via two-proton removal from ^{29}Ne . The beam was produced in a similar manner to that for ^{29}F and the energy was 228 MeV per nucleon with an average intensity of 8×10^3 particles per second.

Unfortunately, in this measurement the cross section for the two-proton removal was much lower than expected and the statistics obtained for $^{24}\text{O}+3n$ coincidence events was too low to be usefully exploited. Nevertheless, the decay of ^{27}O could be identified from the $^{24}\text{O}+2n$ coincidence data. As may be seen in **Extended Data Fig. 2e**, the three-body decay energy (E_{012}) spectrum gated by $E_{01} < 0.08$ MeV – corresponding to selection of the ^{26}O ground-state decay – exhibits a clear peak at around 1 MeV. As the simulations demonstrate, this is consistent with the sequential decay of the ^{27}O resonance observed in the ^{29}F beam data (Fig. 2c).

Invariant-mass method The invariant mass of ^{28}O , $M(^{28}\text{O})$, was reconstructed from the momentum vectors of all the decay particles (^{24}O and $4n$) with $M(^{28}\text{O}) = \sqrt{(\sum E_i)^2 - (\sum \mathbf{p}_i)^2}$, where E_i and \mathbf{p}_i denote the total energy and momentum vector of the decay particles. The decay energy is then obtained as $E_{01234} = M(^{28}\text{O}) - M(^{24}\text{O}) - 4M_n$, where $M(^{24}\text{O})$ and M_n are the masses of ^{24}O and the neutron, respectively. The decay energy resolution is estimated by Monte-Carlo simulations. The resolution (FWHM) varies as a function of the decay energy approximately as $0.14(E_{01234} + 0.87)^{0.81}$ MeV.

Simulations The experimental response functions, for both the full and partial decay energy spectra, were derived from a Monte-Carlo simulation based on GEANT4 (ref.⁵⁶). All relevant characteristics of the setup (geometrical acceptances and detector resolutions) were incorporated, as well as those of the beam, target and reaction effects. The QGSP_INCLXX physics class was adopted to describe the interactions of the neutrons in the detectors (as well as non active material) as it reproduces well the experimentally determined single-neutron detection efficiency as well as the detailed characteristics of neutron crosstalk events^{57,58}. **The generated events treated using the same analysis procedure as for the experimental data.** The overall efficiency as a function of decay energy for detecting ^{24}O and 3 and 4 neutrons, as estimated by the simulations, is shown by the insets of **Extended Data Fig. 1**.

Fitting of decay energy spectra The energies, widths, and amplitudes of the resonances, as modelled by intrinsic lineshapes with a Breit-Wigner form with energy-dependent widths, were obtained via fits of the corresponding decay energy spectra using the maximum likelihood method, where the experimental responses were obtained by the simulations. As the decays of both ^{27}O and ^{28}O proceed via the ^{26}O ground

state (18 keV²⁷), the width of which is very small, the observed widths will be dominated by the one- and two-neutron decay, respectively, to ^{26}O . We assume an E_{01234}^2 dependence of the width for the $2n$ emission⁵⁹ to ^{26}O in the case of ^{28}O and an energy dependence for the width of the single-neutron emission⁶⁰ from ^{27}O to ^{26}O . Fits with orbital angular momentum (L) dependent widths ($L = 2$ and 3) for the latter gave consistent results within the statistical uncertainties.

A non-resonant component is not included in the fitting as it is small, if not negligible, as in the cases of $^{25,26}\text{O}$ produced in one-proton removal reactions in previous experiments^{24–27}. The event selection with $E_{012} < 0.08$ MeV should further reduce any such contribution. As a quantitative check, a fit with a non-resonant component — modelled with a lineshape given by $p_0 \sqrt{E_{0123}} \exp(-p_1 E_{0123})$, where p_0 and p_1 are fitting parameters — has been examined. This gives 8% reduction in the ^{28}O cross section with a very limited impact on the energies and widths of the $^{27,28}\text{O}$ resonances.

Neutron crosstalk A single beam velocity neutron may scatter between individual plastic scintillator detectors of the three neutron walls of the setup. Such crosstalk events can mimic true multi-neutron events and present a source of background. By examining the apparent kinematics of such events and applying so-called causality conditions, this background can be almost completely eliminated^{57,58}. Importantly, both the rejection techniques and the rate and characteristics of the crosstalk have been benchmarked in and compared to the simulations for dedicated measurements with single-neutron beams.

In the case of the 4 neutron detection to identify ^{28}O only some 16% of the events arise from crosstalk which could not be eliminated (Fig. 2a). The vast majority of these residual crosstalk events arise in cases when one (or occasionally more) of the neutrons emitted in the decay of ^{28}O is subject to crosstalk. A very much smaller fraction is also estimated to be produced when one of the three neutrons from the decay of ^{27}O , produced directly by proton and neutron knockout, undergoes crosstalk. Importantly the crosstalk cannot generate a narrow peak-like structure in the E_{01234} decay energy spectrum.

Partial decay energy of subsystems The partial decay energies of the $^{24}\text{O}+xn$ subsystems can be used to investigate the manner in which $^{27,28}\text{O}$ decay. In this analysis the decay neutrons are numbered (n_1, n_2, \dots) by ascending order of two-body relative energy E_{0i} between ^{24}O and n_i – that is, such that, $E_{01} < E_{02} < E_{03} < E_{04}$. Of particular interest here is the extremely low decay energy of the ^{26}O ground state (18 keV²⁷), such that it appears just above zero energy (or neutron-decay threshold) in the two-body partial decay energy E_{01} and three-body partial decay energy (E_{012}).

Extended Data Figs. 2a and b display the distributions of the partial decay energies E_{012} and E_{034} for the $^{24}\text{O}+4n$ coincidence events with a total decay energy $E_{01234} < 1$ MeV. The resulting sharp threshold peak in the E_{012} spectrum is a clear sign of sequential decay through the ^{26}O ground state. This is confirmed quantitatively by a simulation assuming two-neutron emission to the ^{26}O ground state, which in turn decays by two-neutron emission to the ^{24}O ground state, which describes well the E_{012} and E_{034} spectra. By comparison, a simulation assuming five-body phase space decay fails to reproduce both of these spectra. We thus conclude that the ^{28}O ground state sequentially decays via the ^{26}O ground state

as depicted in Fig. 2e.

In a similar vein the sequential decay of ^{27}O through the ^{26}O ground state was identified from the analysis of the partial decay energies for the $^{24}\text{O}+3n$ coincidence events. Extended Data Figs. 2c and d show the distributions of the partial decay energies E_{012} and E_{03} for events for which $1.0 < E_{0123} < 1.2$ MeV. The E_{012} spectrum exhibits a strong enhancement at zero energy indicative of sequential decay through the ^{26}O ground state. This interpretation is confirmed by the comparison shown with a simulation for the sequential decay of ^{27}O including the contribution from the decay of ^{28}O .

Widths of the $^{27,28}\text{O}$ resonances As the energy of the ^{28}O resonance is lower than those of ^{27}O and ^{25}O (Fig. 2e), both one- and three-neutron emission are energetically forbidden. The two-neutron decay to the ^{26}O ground state and the four-neutron decay to ^{24}O are allowed with nearly equal decay energies. The former decay should be favoured as the effective few-body centrifugal barrier increases according to the number of emitted particles⁵⁹. It may be noted that the upper limit of 0.7 MeV observed here for the ^{28}O resonance width is consistent with the theoretical estimates for its sequential decay⁵⁹.

The upper limit for the ^{27}O width (0.18 MeV) may be compared to the single-particle widths⁶¹ for neutron decay. Since the width of ^{26}O is very narrow due to the extremely small decay energy (18 keV²⁷), the ^{27}O width should be dominated by the one for the first step $^{27}\text{O} \rightarrow ^{26}\text{O}+n$. The widths for s , p , d , f -wave neutron emission are 5, 3, 0.8, 0.06 MeV. Assuming that the corresponding spectroscopic factors are not small (≥ 0.1), this would suggest that the decay occurs via d - or f -wave neutron emission. As such, the spin and parity of the ^{27}O resonance may be tentatively assigned to be $3/2^+$ or $7/2^-$.

Momentum distribution Extended Data Fig. 4 shows the transverse momentum (P_x) distribution of the $^{24}\text{O}+3n$ system in the rest frame of the ^{29}F beam for events gated by $E_{012} < 0.08$ MeV and $E_{0123} < 0.8$ MeV – that is, events corresponding to population of the ^{28}O ground state. We note that this analysis employed the $^{24}\text{O}+3n$ events as the limited $^{24}\text{O}+4n$ statistics could not be usefully exploited in distinguishing between the momentum distributions for the proton knockout from different orbitals. Even though the momentum distribution is slightly broadened by the undetected decay neutron, it still reflects directly the character of the knocked-out proton.

The experimental P_x distribution is compared to DWIA (Distorted Wave Impulse Approximation) reaction theory calculations (see below) for knockout of a proton from the $1d_{5/2}$ and $2s_{1/2}$ orbitals. The theoretical distributions are convoluted with the experimental resolution as well as the much smaller broadening induced by the undetected neutron ($\sigma = 34$ MeV/c). The best fit normalization of the theoretical distribution obtained by the distorting potential with the Dirac phenomenology (microscopic folding model potential) through a χ^2 minimization gives reduced- χ^2 values of 2.0 (2.0) for the $1d_{5/2}$ proton knockout and 3.7 (4.7) for the $2s_{1/2}$ knockout. The curves in Extended Data Fig. 4 represent the calculations obtained by the distorting potential with the Dirac phenomenology. The better agreement for the $1d_{5/2}$ proton knockout **suggests** that the spin and parity of the ^{29}F ground state is $5/2^+$ as predicted by the shell model calculations, including those using the EEdf3 interaction.

EEdf3 calculations The EEdf3 Hamiltonian³² is a variant of the EEdf1 Hamiltonian, which was used in ref.³³ for describing F, Ne, Na, and Mg isotopes up to neutron dripline³². The EEdf1 Hamiltonian was derived from chiral effective field theory (χ EFT) interaction, as described below. The χ EFT interaction proposed by Entem and Machleidt^{62,63} was taken with $\Lambda = 500$ MeV, as the nuclear force in vacuum, up to the next-to-next-to-next-to-leading-order (N^3LO) in the χ EFT. It was then renormalized using the V_{low-k} approach^{64,65} with a cutoff of $\Lambda_{V_{low-k}} = 2.0$ fm⁻¹, in order to obtain a low-momentum interaction decoupled from high-momentum phenomena. The EKK method^{66–68} was then adopted in order to obtain the effective NN interaction for the sd - pf shells, by including the so-called \hat{Q} -box, which incorporates unfolded effects coming from outside of the model space⁶⁹, up to third order and its folded diagrams. As to the single-particle basis vectors, the eigenfunctions of the three-dimensional harmonic oscillator potential were taken as usual. In addition, the contributions from the Fujita Miyazawa three-nucleon force (3NF)⁷⁰ were added in the form of the effective NN interaction⁴¹. The Fujita Miyazawa force represents the effects of the virtual excitation of a nucleon to a Δ baryon by pion-exchange processes and includes the effects of Δ -hole excitations, but does not include other effects such as contact (c_D and c_E) terms.

In the present study, we explicitly treat neutrons only, while the protons remained confined to the ^{16}O closed-shell core. As such, there is no proton-neutron interaction between active nucleons, and the neutron-neutron interaction is weaker. As this increases the relative importance of the effects from 3NF, we adopt the more modern 3NF of Hebeler et al.⁴⁴, which is expected to have finer details and improved properties. We obtain effective NN interactions from this 3NF first by deriving density-dependent NN interactions from them⁷¹ and then by having the density dependence integrated out with the normal density. It was suggested that this 3NF produces results similar to those reported in ref.³³ for the F, Ne, Na and Mg isotopes. As a result of this change, the single-particle energies are shifted for the $1d_{5/2}$ and $2s_{1/2}$ orbitals by -0.72 MeV, for the $1d_{3/2}$ orbital by -0.42 MeV and for the pf shell orbitals by 0.78 MeV.

Coupled-cluster calculations and emulators The starting point for the calculations is the intrinsic Hamiltonian,

$$H = T_{\text{kin}} - T_{\text{CoM}} + V_{NN} + V_{NNN}. \quad (1)$$

Here T_{kin} is the kinetic energy, T_{CoM} the kinetic energy of the center-of-mass, and $V_{NN} + V_{NNN}$ are nucleon-nucleon and three-nucleon potentials from χ EFT^{62,72,73} and include Delta isobars⁷⁴. The momentum space cutoff of this interaction is $\Lambda = 394$ MeV/c.

We used the coupled-cluster method^{75–81} with singles-doubles and perturbative triples excitations, known as the CCSDT-3 approximation^{82,83}, to compute the ground-state energy of ^{28}O , and the particle-removed equation-of-motion (EOM) coupled-cluster method from refs.^{84,85} for the ground-state energy of ^{27}O . The coupled-cluster calculations start from a spherical Hartree-Fock reference of ^{28}O in a model-space of 13 major harmonic oscillator shells with an oscillator frequency of $\hbar\omega = 16$ MeV. The three-nucleon force is limited to three-body energies up to $E_{3\text{max}} = 14\hbar\omega$. For energy differences the effects of model-space truncations and coupling to the scattering continuum are small and were neglected in the

777 history matching analysis.

778 The low-energy constants (LECs) of this interaction are
 779 constrained by a history matching approach employing high-
 780 precision emulators enabled by eigenvector continuation⁸⁶.
 781 These tools mimic the results of actual coupled-cluster com-
 782 putations, but are several orders of magnitude faster to eval-
 783 uate, hence facilitating comprehensive exploration of the rel-
 784 evant parameter space. The emulators work as follows. In
 785 the 17-dimensional space of LECs, the parameterization of
 786 the $\Delta\text{NNLO}_{\text{GO}}(394)$ potential⁷⁴ serves as a starting point
 787 around which we select emulator training points according to
 788 a space-filling lattice hypercube design for which we perform
 789 coupled-cluster computations of ground-state energies, radii,
 790 and excited states of $^{16,22,24}\text{O}$ (see Extended Data Table 1 for
 791 details). Keeping track of the variations of the observables
 792 and the corresponding coupled-cluster eigenstates as the low-
 793 energy constants are varied, allows us to construct an emu-
 794 lator that can be used to predict the results for novel param-
 795 eterizations. This emulator strategy is rather general⁸⁷ and
 796 possible because the eigenvector trajectory generated by con-
 797 tinuous changes of the low-energy constants only explores a
 798 relatively small subspace of Hilbert space. Eigenvector con-
 799 tinuation emulation tailored to coupled-cluster eigenstates is
 800 referred to as the subspace-projected coupled-cluster (SP-CC)
 801 method. In this work, we extended the SP-CC method of
 802 ref.⁸⁸ to excited states and increased the precision by includ-
 803 ing triples excitations via the CCSDT-3 and EOM-CCSDT-3
 804 methods, respectively. Our SP-CC emulators employ up to 68
 805 training points for each observable of interest, and use model
 806 spaces consisting of 11 major harmonic oscillator shells. We
 807 checked the precision of each emulator by performing emula-
 808 tor diagnostics⁸⁹: confronting the emulator predictions with
 809 the results of actual coupled-cluster computations, see Ex-
 810 tended Data Fig. 5. Once constructed, the emulators are in-
 811 expensive computational tools that can precisely predict the
 812 results for virtually arbitrary parameterizations of the EFT po-
 813 tentials. This allows us to explore several hundred million
 814 parameterizations with the computational cost of only a few
 815 hundred actual coupled-cluster computations. The use of emu-
 816 lation hence represents a critical advance, that facilitates a far
 817 deeper analysis of the coupled-cluster method, that was previ-
 818 ously infeasible due to the substantial computational expense
 819 of the coupled-cluster calculations. Hence, these techniques
 820 overcome a major barrier to the use of such coupled-cluster
 821 methods.

822 **Coupled-cluster calculations: Linking models to reality**
 823 We describe the relationship between experimental observa-
 824 tions, z , and *ab initio* model predictions $M(\theta)$, where θ de-
 825 notes the parameter vector of the theoretical model, as

$$z = M(\theta) + \epsilon_{\text{method}} + \epsilon_{\text{model}} + \epsilon_{\text{exp}}. \quad (2)$$

826 In this relation, we consider experimental uncertainties, ϵ_{exp} ,
 827 as well as method approximation errors ϵ_{method} . The latter
 828 represent, e.g., model-space truncations and other approxima-
 829 tions in the *ab initio* many-body solvers and are estimated
 830 from method convergence studies⁷⁴. Most importantly, we
 831 acknowledge the fact that even if we were to evaluate the
 832 model $M(\theta)$ at its best possible choice of the parameter vec-
 833 tor, θ^* , the model output, $M(\theta^*)$, would still not be in ex-
 834 act quantitative agreement with reality due to, e.g., simplifi-
 835 cations and approximations inherent to the model. We de-
 836 scribe this difference in terms of a model discrepancy term,

837 ϵ_{model} . The expected EFT-convergence pattern of our model
 838 allows us to specify further probabilistic attributes of ϵ_{model}
 839 a priori^{90–93}. We employ the model errors defined in⁹⁴. The
 840 use of emulators based on eigenvector continuation^{86–88} pro-
 841 vides us with an efficient approximation, $\tilde{M}(\theta)$, of the model.
 842 This approach entails an emulator error $\epsilon_{\text{emulator}}$ such that
 843 $M(\theta) = \tilde{M}(\theta) + \epsilon_{\text{emulator}}$, as outlined in the previous section.
 844 Obviously, we do not know the exact values of the errors in
 845 Eq. (2), hence we represent them as uncertain quantities and
 846 specify reasonable forms for their statistical distributions, in
 847 alignment with the Bayesian paradigm. This allows for these
 848 uncertainties to be formally incorporated in all subsequent cal-
 849 culations and inferences. We also assume that the errors add
 850 independently of each other and the inputs θ .

851 **Coupled-cluster calculations: History matching** In this
 852 work we use an iterative approach for complex computer mod-
 853 els known as history matching (HM)^{45–47} in which the model,
 854 solved at different fidelities, is confronted with experimental
 855 data z using relation (2). The aim of HM is to estimate the
 856 set $\mathcal{Q}(z)$ of values for θ , for which the evaluation of a model
 857 $M(\theta)$ yields an acceptable—or at least not implausible (NI)—
 858 match to a set of observations z . HM has been employed in
 859 various studies^{95–97} ranging, e.g., from effects of climate mod-
 860 eling^{98,99} to systems biology⁴⁷. The present work represents
 861 the first application in nuclear physics. We introduce the stan-
 862 dard implausibility measure

$$I^2(\theta) = \max_{i \in \mathcal{Z}} \frac{|\tilde{M}_i(\theta) - z_i|^2}{\text{Var}(\tilde{M}_i(\theta) - z_i)}, \quad (3)$$

863 which is a function over the input parameter space and quan-
 864 tifies the (mis-)match between our (emulated) model output
 865 $\tilde{M}_i(\theta)$ and the observation z_i for all observables i in the tar-
 866 get set \mathcal{Z} . This specific definition uses the maximum of the
 867 individual implausibility measures (one for each observable)
 868 as the restricting quantity. We consider a particular value for
 869 θ as implausible if $I(\theta) > c_I \equiv 3.0$ appealing to Pukelsheim’s
 870 three-sigma rule¹⁰⁰. In accordance with the assumptions lead-
 871 ing to Eq. (2), the variance in the denominator of Eq. (3) is a
 872 sum of independent squared errors. Generalizations of these
 873 assumptions are straightforward if additional information on
 874 error covariances or possible inaccuracies in our error model
 875 would become available. An important strength of the HM
 876 approach is that we can proceed iteratively, excluding regions
 877 of input space by imposing cutoffs on implausibility measures
 878 that can include *additional* observables z_i and corresponding
 879 model outputs M_i , and possibly refined emulators \tilde{M}_i , as the
 880 iterations proceed. The iterative HM proceeds in waves ac-
 881 cording to a straightforward strategy that can be summarized
 882 as follows:

- 883 1. At iteration j : Evaluate a set of model runs over the
 884 current NI volume \mathcal{Q}_j using a space-filling design of
 885 sample values for the parameter inputs θ . Choose a re-
 886 jection strategy based on implausibility measures for a
 887 set \mathcal{Z}_j of informative observables.
- 888 2. Construct or refine emulators for the model predictions
 889 across the current non-implausible volume \mathcal{Q}_j .
- 890 3. The implausibility measures are then calculated over
 891 \mathcal{Q}_j , using the emulators, and implausibility cutoffs are
 892 imposed. This defines a new, smaller NI volume \mathcal{Q}_{j+1}
 893 which should satisfy $\mathcal{Q}_{j+1} \subset \mathcal{Q}_j$.

894 4. Unless (a) the emulator uncertainties for all observ-
 895 ables of interest are sufficiently small in comparison to
 896 the other sources of uncertainty, (b) computational re-
 897 sources are exhausted, or (c) all considered points in
 898 the parameter space are deemed implausible, we:

- 899 – include any additional informative observables in
 900 the considered set \mathcal{Z}_{j+1} , and return to step 1.

901 5. If 4(a) or (b) is true we generate a large number of ac-
 902 ceptable runs from the final NI volume $\mathcal{Q}_{\text{final}}$, sampled
 903 according to scientific need.

904 The *ab initio* model for the observables we consider comprises
 905 at most 17 parameters; 4 subleading pion-nucleon couplings,
 906 11 nucleon-nucleon contact couplings, and 2 short-ranged
 907 three-nucleon couplings. To identify a set of NI parameter
 908 samples we performed iterative HM in four waves using ob-
 909 servables and implausibility measures as summarized in Ex-
 910 tended Data Table 1. For each wave we employ a sufficiently
 911 dense latin hypercube set of several million candidate param-
 912 eter samples. For the model evaluations we utilized fast com-
 913 putations of neutron-proton (*np*) scattering phase shifts and
 914 efficient emulators for the few- and many-body observables
 915 listed. See Extended Data Table 2 for the list of included ob-
 916 servables and key information for each wave. The input vol-
 917 ume for wave 1 included large ranges for the relevant param-
 918 eters, as indicated by the panel ranges in the lower left triangle
 919 of Extended Data Fig. 6. In all four waves, the input volume
 920 for $c_{1,2,3,4}$ is a four-dimensional hypercube mapped onto the
 921 multivariate Gaussian pdf resulting from a Roy-Steiner analy-
 922 sis of πN scattering data¹⁰¹. In wave 1 and wave 2 we sampled
 923 all relevant parameter directions for the set of included two-
 924 nucleon observables. In wave 3, the additional ³H and ⁴He
 925 observables were added. Since they are known to be rather
 926 insensitive to the four model parameters acting solely in the
 927 *P*-wave, we therefore ignored this subset of the inputs and
 928 compensated by slightly enlarging the corresponding method
 929 errors. This is a well-known emulation procedure called in-
 930 active parameter identification⁴⁵. For the final iteration, i.e.
 931 wave 4, we considered all 17 model parameters and added a
 932 set of observables for the oxygen isotopes ^{16,22,24}O and emu-
 933 lated the model outputs for 5×10^8 parameter samples. Ex-
 934 tended Data Fig. 6 summarizes the sequential NI volume re-
 935 duction, wave-by-wave, and indicates the set \mathcal{Q}_4 of 634 NI
 936 samples after the fourth and final wave. The volume reduc-
 937 tion is guided by the implausibility measure (3) and the op-
 938 tical depths (see Eqs. (25) and (26) in ref.⁴⁷), where the lat-
 939 ter are illustrated in the lower left triangle of Extended Data
 940 Fig. 6. The NI samples summarise the parameter region of
 941 interest, and can directly aid insight regarding interdependen-
 942 cies between parameters induced by the match to observed
 943 data. This region is also where we would expect the poste-
 944 rior distribution to reside. We see that the iterative history
 945 matching process trains a nested series of emulators that be-
 946 come more and more accurate over this posterior region, as
 947 the iterations progress.

948 **Coupled-cluster calculations: Bayesian posterior sam-**
 949 **pling** The NI samples in the final HM wave also serve as
 950 excellent starting points for extracting the posterior probabili-
 951 ty density function (pdf) of the parameters θ , i.e. $p(\theta|A =$
 952 $2 - 24)$. To this end, we assume a normally distributed likeli-
 953 hood, according to Eq. (2), and a uniform prior corresponding
 954 to the initial volume of wave 1. Note that the prior for $c_{1,2,3,4}$

955 is the multivariate Gaussian resulting from a Roy-Steiner anal-
 956 ysis of πN scattering data¹⁰¹. We sample the posterior using
 957 the affine invariant Markov Chain Monte Carlo ensemble sam-
 958 pler emcee¹⁰² and the resulting distribution is shown in the up-
 959 per right triangle of Extended Data Fig. 6. The sampling was
 960 performed with four independent ensemble chains, each with
 961 150 walkers, and satisfactory convergence was reached (diag-
 962 nosed using the Gelman-Rubin test with $|\hat{R} - 1| < 10^{-4}$ in all
 963 dimensions). We performed $5 \cdot 10^5$ iterations per walker—after
 964 an initial warm-up of 5000 steps—and kept one final sample
 965 for every 500 steps. Combining all chains we therefore end up
 966 with $4 \times 150 \times 1000 = 6 \cdot 10^5$ final samples. In addition, we
 967 explored the sensitivity of our results to modifications of the
 968 likelihood definition. Specifically, we used a student-t distri-
 969 bution ($\nu = 5$) to see the effects of allowing heavier tails, and
 970 we introduced an error covariance matrix to study the effect
 971 of correlations ($\rho \approx 0.6$) between selected observables. In the
 972 end, the differences in the extracted credibility regions was not
 973 great and we therefore present only results obtained with the
 974 uncorrelated, multivariate normal distribution (see Extended
 975 Data Table 3).

976 A subset of marginal posterior predictive distributions (ppd)
 977 are shown in Extended Data Fig. 7. Clearly, a subset of 100
 978 samples provides an accurate low-statistics representation of
 979 this marginalized ppd. We exploit this feature in our final pre-
 980 dictions for ^{27,28}O presented in the main text. Note that the
 981 ppd does not include draws from the model discrepancy pdf.
 982 To include information about the ²⁵O separation energy with
 983 respect to ²⁴O we perform a straightforward Bayesian update
 984 of the posterior pdf $p(\theta|A = 2 - 24)$ for the LECs. This com-
 985 plements the statistical analysis of the *ab initio* model with
 986 important information content from an odd and neutron-rich
 987 oxygen isotope. Using the pdf $p(\theta|A = 2 - 24)$ we draw
 988 500 model predictions for $\Delta E(^{25,24}\text{O})$ and account for all in-
 989 dependent and normally distributed uncertainties according to
 990 Extended Data Table 1. Next, we draw 121 different LEC pa-
 991 rameterizations from the updated posterior and use coupled
 992 cluster to compute the corresponding ground-state energies of
 993 ^{27,28}O. The full bivariate ppd for the ²⁸O-²⁴O and ²⁷O-²⁸O
 994 energy differences, $\Delta E(^{28,24}\text{O})$ and $\Delta E(^{27,28}\text{O})$, with asso-
 995 ciated credible regions, are shown in Extended Data Fig. 3.
 996 The effect of the continuum on the energy difference was es-
 997 timated to be ~ 0.5 MeV in ref.³⁹ and was neglected in this
 998 work. We note that our ability to examine the full ppd for these
 999 expensive *ab initio* calculations provides welcome additional
 1000 insight, which is a direct consequence of the use of the HM
 1001 procedure. We note that a sufficiently precise determination
 1002 of $\Delta E(^{28,24}\text{O})$ and $\Delta E(^{27,28}\text{O})$ requires wave 4 in the history
 1003 matching and also using the separation energy $\Delta E(^{24,25}\text{O})$ for
 1004 the construction of the pdf. Without input about ²⁵O, the sep-
 1005 aration energy $\Delta E(^{27,28}\text{O})$ becomes too uncertain to be use-
 1006 ful. It is in this sense that a sufficiently precise prediction
 1007 of $\Delta E(^{27,28}\text{O})$ is finely tuned and cannot be based only on
 1008 the properties of light nuclei up to ⁴He. Changes in the low-
 1009 energy constants that have small impact in few nucleon sys-
 1010 tems are magnified in ²⁸O. Apparently, one needs information
 1011 about all nuclear shells including the *sd* shell to meaningfully
 1012 predict this key nucleus.

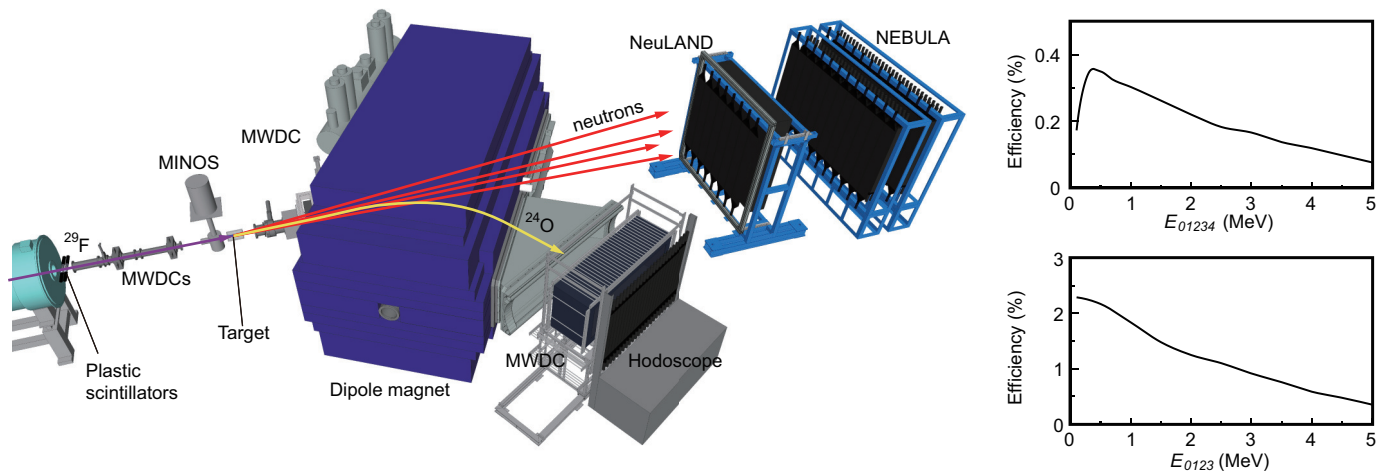
1013 **DWIA calculations** The distorted-wave impulse approx-
 1014 imation (DWIA)^{53,103,104} describes proton-induced proton
 1015 knockout – (*p, 2p*) – processes as proton-proton (*pp*) elas-
 1016 tic scattering. This is referred to as the impulse approxima-

- tion, which is considered to be valid at intermediate energies when both outgoing protons have large momenta with respect to the residual nucleus. The DWIA approach has been successful in describing proton-induced knockout reactions; in ref.⁵³, it was shown that the spectroscopic factors deduced from $(p, 2p)$ reactions for the single-particle levels near the Fermi surface of several nuclei are consistent with those extracted from electron-induced $(e, e'p)$ reactions. The transition matrix of $(p, 2p)$ processes within DWIA theory is given by $T_{p2p} = \langle \chi_1 \chi_2 | t_{pp} | \chi_0 \phi_p \rangle$, where χ_i are the distorted waves of the incoming proton (0) and the outgoing two protons (1 and 2), whereas ϕ_p is the normalized bound-state wave function of the proton inside the nucleus. The pp effective interaction is denoted by t_{pp} , the absolute square of which is proportional to the pp elastic cross section. The nonlocality corrections¹⁰⁵ to both χ_i and ϕ_p are taken into account as well as the Moller factor¹⁰⁶ for t_{pp} that guarantees the Lorentz invariance of the pp reaction probability. The $(p, 2p)$ cross section is given by $F_{\text{kin}} C^2 S |T_{p2p}|^2$ with F_{kin} being a kinetic factor and $C^2 S$ the spectroscopic factor.
- In this study, the cross section integrated over the allowed kinematics of the outgoing particles was calculated. We employed the Franey-Love parameterization¹⁰⁷ for t_{pp} and the Bohr-Mottelson's (BM) single-particle potential¹⁰⁸ in order to compute ϕ_p . We have used two types of the one-body distorting potential to obtain χ – specifically, the Dirac phenomenology (set EDAD2¹⁰⁹) and a microscopic folding model potential based on the Melbourne G -matrix interaction¹¹⁰ and one-body nuclear densities calculated with the BM single-particle model¹⁰⁸. It was found that the difference in the $(p, 2p)$ cross sections calculated with the two sets of distorting potentials was at most 7.5%. In addition, they give almost identical shapes for the momentum distributions. As such, we have adopted here the average value of the cross sections for each single-particle configuration.
- Data availability** Source data for Figs. 2a-c, Extended Data Figs. 2a-f, and Extended Data Fig. 4 are provided with this paper. All of the other relevant data that support the findings of this study are available from the corresponding author upon reasonable request.
- Code availability** Our unpublished computer codes used to generate the results reported in this paper are available from the corresponding author upon reasonable request.
- ## References
55. Kubo, T. *et al.* BigRIPS separator and ZeroDegree spectrometer at RIKEN RI Beam Factory. *Prog. Theor. Exp. Phys.* **2012**, 03C003 (2012).
 56. Agostinelli, S. *et al.* GEANT4—a simulation toolkit. *Nucl. Instrum. Methods Phys. Res. Sect. A* **506**, 250–303 (2003).
 57. Nakamura, T. & Kondo, Y. Large acceptance spectrometers for invariant mass spectroscopy of exotic nuclei and future developments. *Nucl. Instrum. Methods Phys. Res., Sect. B* **376**, 156–161 (2016).
 58. Kondo, Y., Tomai, T. & Nakamura, T. Recent progress and developments for experimental studies with the SAMURAI spectrometer. *Nucl. Instrum. Methods Phys. Res., Sect. B* **463**, 173–178 (2020).
 59. Grigorenko, L. V., Mukha, I. G., Scheidenberger, C. & Zhukov, M. V. Two-neutron radioactivity and four-nucleon emission from exotic nuclei. *Phys. Rev. C* **84**, 021303 (2011).
 60. Lane, A. M. & Thomas, R. G. R-Matrix Theory of Nuclear Reactions. *Rev. Mod. Phys.* **30**, 257–353 (1958).
 61. Dover, C. B., Mahaux, C. & Weidenmüller, H. A. The single-particle limit for partial widths. *Nucl. Phys. A* **139**, 593–604 (1969).
 62. Machleidt, R. & Entem, D. Chiral effective field theory and nuclear forces. *Phys. Rep.* **503**, 1–75 (2011).
 63. Entem, D. R. & Machleidt, R. Accurate charge-dependent nucleon-nucleon potential at fourth order of chiral perturbation theory. *Phys. Rev. C* **68**, 041001 (2003).
 64. Bogner, S., Kuo, T. T. S., Coraggio, L., Covello, A. & Itaco, N. Low momentum nucleon-nucleon potential and shell model effective interactions. *Phys. Rev. C* **65**, 051301 (2002).
 65. Nogga, A., Bogner, S. K. & Schwenk, A. Low-momentum interaction in few-nucleon systems. *Phys. Rev. C* **70**, 061002 (2004).
 66. Takayanagi, K. Effective interaction in non-degenerate model space. *Nucl. Phys. A* **852**, 61–81 (2011).
 67. Takayanagi, K. Effective Hamiltonian in the extended Krenciglowa-Kuo method. *Nucl. Phys. A* **864**, 91–112 (2011).
 68. Tsunoda, N., Takayanagi, K., Hjorth-Jensen, M. & Otsuka, T. Multi-shell effective interactions. *Phys. Rev. C* **89**, 024313 (2014).
 69. Hjorth-Jensen, M., Kuo, T. T. & Osnes, E. Realistic effective interactions for nuclear systems. *Phys. Rep.* **261**, 125–270 (1995).
 70. Fujita, J. & Miyazawa, H. Pion theory of three-body forces. *Prog. Theor. Phys.* **17**, 360 (1957).
 71. Kohno, M. Nuclear and neutron matter G -matrix calculations with a chiral effective field theory potential including effects of three-nucleon interactions. *Phys. Rev. C* **88**, 064005 (2013). ; erratum **96**, 059903 (2017).
 72. van Kolck, U. Few-nucleon forces from chiral Lagrangians. *Phys. Rev. C* **49**, 2932–2941 (1994).
 73. Epelbaum, E., Hammer, H.-W. & Meißner, U.-G. Modern theory of nuclear forces. *Rev. Mod. Phys.* **81**, 1773–1825 (2009).
 74. Jiang, W. G. *et al.* Accurate bulk properties of nuclei from $A = 2$ to ∞ from potentials with Δ isobars. *Phys. Rev. C* **102**, 054301 (2020).
 75. Coester, F. Bound states of a many-particle system. *Nucl. Phys.* **7**, 421–424 (1958).
 76. Coester, F. & Kümmel, H. Short-range correlations in nuclear wave functions. *Nucl. Phys.* **17**, 477–485 (1960).
 77. Kümmel, H., Lührmann, K. H. & Zabolitzky, J. G. Many-fermion theory in expS- (or coupled cluster) form. *Phys. Rep.* **36**, 1–63 (1978).
 78. Mihaïla, B. & Heisenberg, J. H. Microscopic Calculation of the Inclusive Electron Scattering Structure Function in ^{16}O . *Phys. Rev. Lett.* **84**, 1403–1406 (2000).
 79. Dean, D. J. & Hjorth-Jensen, M. Coupled-cluster approach to nuclear physics. *Phys. Rev. C* **69**, 054320 (2004).
 80. Bartlett, R. J. & Musiał, M. Coupled-cluster theory in quantum chemistry. *Rev. Mod. Phys.* **79**, 291–352 (2007).
 81. Hagen, G., Papenbrock, T., Hjorth-Jensen, M. & Dean, D. J. Coupled-cluster computations of atomic nuclei. *Rep. Prog. Phys.* **77**, 096302 (2014).
 82. Noga, J., Bartlett, R. J. & Urban, M. Towards a full CCSDT model for electron correlation. CCSDT-n models. *Chem. Phys. Lett.* **134**, 126–132 (1987).
 83. Watts, J. D. & Bartlett, R. J. Iterative and non-iterative triple excitation corrections in coupled-cluster methods for excited electronic states: the EOM-CCSDT-3 and EOM-CCSD(\bar{T}) methods. *Chem. Phys. Lett.* **258**, 581–588 (1996).
 84. Gour, J. R., Piecuch, P., Hjorth-Jensen, M., Włoch, M. & Dean, D. J. Coupled-cluster calculations for valence systems around ^{16}O . *Phys. Rev. C* **74**, 024310 (2006).
 85. Morris, T. D. *et al.* Structure of the Lightest Tin Isotopes. *Phys. Rev. Lett.* **120**, 152503 (2018).
 86. Frame, D. *et al.* Eigenvector Continuation with Subspace Learning. *Phys. Rev. Lett.* **121**, 032501 (2018).

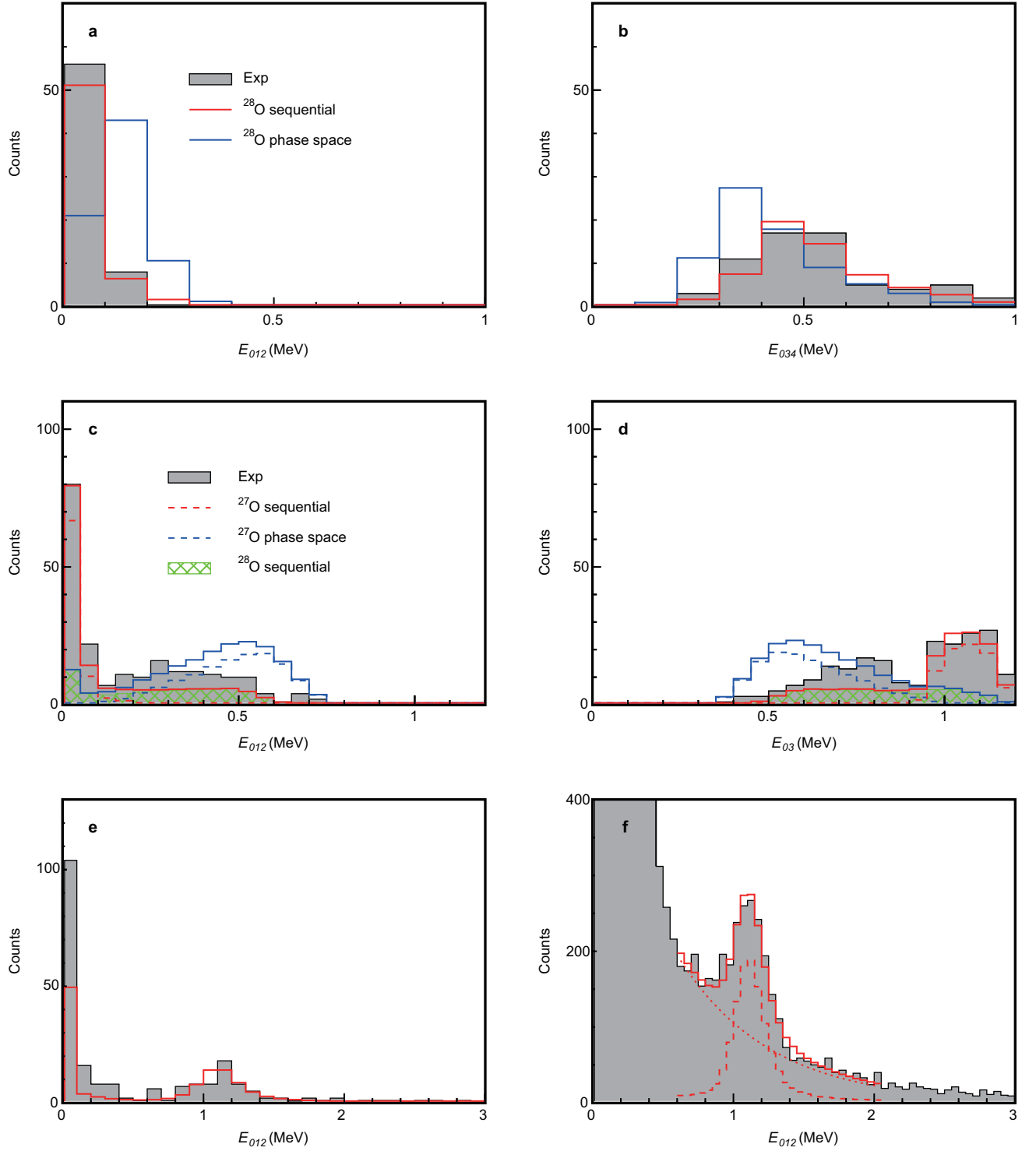
- 1146 87. König, S., Ekström, A., Hebeler, K., Lee, D. & Schwenk, A. Eigenvector continuation as an efficient and accurate emulator for uncertainty quantification. *Phys. Lett. B* **810**, 135814 (2020).
- 1148 88. Ekström, A. & Hagen, G. Global Sensitivity Analysis of Bulk Properties of an Atomic Nucleus. *Phys. Rev. Lett.* **123**, 252501 (2019).
- 1152 89. Bastos, L. S. & O’Hagan, A. Diagnostics for Gaussian Process Emulators. *Technometrics* **51**, 425–438 (2009).
- 1154 90. Wesolowski, S., Klco, N., Furnstahl, R., Phillips, D. & Thapaliya, A. Bayesian parameter estimation for effective field theories. *J. Phys. G* **43**, 074001 (2016).
- 1157 91. Melendez, J., Wesolowski, S. & Furnstahl, R. Bayesian truncation errors in chiral effective field theory: nucleon-nucleon observables. *Phys. Rev. C* **96**, 024003 (2017).
- 1160 92. Wesolowski, S., Furnstahl, R., Melendez, J. & Phillips, D. Exploring Bayesian parameter estimation for chiral effective field theory using nucleon–nucleon phase shifts. *J. Phys. G* **46**, 045102 (2019).
- 1164 93. Melendez, J., Furnstahl, R., Phillips, D., Pratola, M. & Wesolowski, S. Quantifying Correlated Truncation Errors in Effective Field Theory. *Phys. Rev. C* **100**, 044001 (2019).
- 1167 94. Ekström, A., Hagen, G., Morris, T. D., Papenbrock, T. & Schwartz, P. D. Δ isobars and nuclear saturation. *Phys. Rev. C* **97**, 024332 (2018).
- 1170 95. Raftery, A. E., Givens, G. H. & Zeh, J. E. Inference from a Deterministic Population Dynamics Model for Bowhead Whales. *J. Am. Stat. Assoc.* **90**, 402–416 (1995).
- 1173 96. Vernon, I., Goldstein, M. & Bower, R. G. Rejoinder. *Bayesian Anal.* **5**, 697–708 (2010).
- 1175 97. Andrianakis, I. *et al.* Bayesian history matching of complex infectious disease models using emulation: a tutorial and a case study on HIV in Uganda. *PLoS Comput Biol.* **11**, e1003968 (2015).
- 1179 98. Williamson, D. *et al.* History matching for exploring and reducing climate model parameter space using observations and a large perturbed physics ensemble. *Clim. Dyn.* **41**, 1703 (2013).
- 1182 99. Edwards, T. L. *et al.* Revisiting Antarctic ice loss due to marine ice-cliff instability. *Nature* **566**, 58–64 (2019).
- 1184 100. Pukelsheim, F. The Three Sigma Rule. *The American Statistician* **48**, 88–91 (1994).
- 1186 101. Siemens, D. *et al.* Reconciling threshold and subthreshold expansions for pion-nucleon scattering. *Phys. Lett. B* **770**, 27–34 (2017).
- 1189 102. Foreman-Mackey, D., Hogg, D. W., Lang, D. & Goodman, J. emcee: The MCMC Hammer. *Publications of the Astronomical Society of the Pacific* **125**, 306–312 (2013).
- 1192 103. Jacob, G. & Maris, T. A. J. Quasi-free scattering and nuclear structure. *Rev. Mod. Phys.* **38**, 121–142 (1966).
- 1194 104. Jacob, G. & Maris, T. A. J. Quasi-free scattering and nuclear structure. II. *Rev. Mod. Phys.* **45**, 6–21 (1973).
- 1196 105. Perey, F. & Buck, B. A non-local potential model for the scattering of neutrons by nuclei. *Nucl. Phys.* **32**, 353–380 (1962).
- 1198 106. Møller, C. General properties of the characteristic matrix in the theory of elementary particles. *Kgl. Danske Videnskab. Selskab, Mat-fys. Medd.*, 1 (1945).
- 1201 107. Franey, M. A. & Love, W. G. Nucleon-nucleon t-matrix interaction for scattering at intermediate energies. *Phys. Rev. C* **31**, 488–498 (1985).
- 1204 108. Bohr, A. & Mottelson, B. R. *NUCLEAR STRUCTURE*. Vol. I (Benjamin, 1969).
- 1206 109. Cooper, E. D., Hama, S., Clark, B. C. & Mercer, R. L. Global Dirac phenomenology for proton-nucleus elastic scattering. *Phys. Rev. C* **47**, 297–311 (1993).
- 1209 110. Amos, K., Dortmans, P., von Geramb, H., Karataglidis, S. & Raynal, J. *ADVANCES IN NUCLEAR PHYSICS*. edited by J.W. Negele and E. Vogt, (Plenum, New York 2000).
- 1212 **Acknowledgement** We thank the RIKEN Nishina Center and the Center for Nuclear Study, the University of Tokyo ac-
- 1214 celerator staff for the excellent beam delivery. This work was supported in part by JSPS KAKENHI Grants No. 18K03672. and No. 18H05404. This work was also supported by the Deutsche Forschungsgemeinschaft (DFG, German Research Foundation) - Proj.- ID 279384907 - SFB 1245, the GSI-TU Darmstadt cooperation agreement, the GSI under contract KZILGE1416, the German Federal Ministry for Education and Research (BMBF) under contract No. 05P15RDFN1 and 05P21PKFN1, the European Research Council (ERC) under the European Union’s Horizon 2020 research and innovation programme (grant agreement numbers 758027 and 258567), the Swedish Research Council grant number 2011-5324, 2017-03839 and 2017-04234. Partial support was also supplied by the Franco-Japanese LIA-International Associated Laboratory for Nuclear Structure Problems as well as the French ANR-14-CE33-0022-02 EXPAND. This work was also supported in part by the Institute for Basic Science (IBS-R031-D1) in Korea and the U.S. Department of Energy, Office of Science, Office of Nuclear Physics, under Award Nos. DE-FG02-96ER40963 and DE-SC0018223. This work was also supported in part by the National Science Foundation, USA under Grant No. PHY-1102511. Computer time was provided by the Innovative and Novel Computational Impact on Theory and Experiment (INCITE) program. This research employed resources of the Oak Ridge Leadership Computing Facility at the Oak Ridge National Laboratory, which is supported by the Office of Science of the U.S. Department of Energy under Contract No. DE-AC05-00OR22725, and resources provided by the Swedish National Infrastructure for Computing (SNIC) at Chalmers Centre for Computational Science and Engineering (C3SE), and the National Supercomputer Centre (NSC) partially funded by the Swedish Research Council. Y.T. acknowledges the support of the JSPS Grant-in-Aid for Scientific Research Grants No. JP21H01114. I.G. has been supported by HIC for FAIR and Croatian Science Foundation under projects no. 1257 and 7194. Z.D. and D.S. have been supported by the National Research, Development and Innovation Fund of Hungary via project No. TKP2021-NKTA-42 and K128947. T.O., N.S., N.T., Y.U., and S.Y. acknowledge valuable support from the “Priority Issue on post-K computer” (hp190160), “Program for Promoting Researches on the Supercomputer Fugaku” (JP-MXP1020200105, hp200130, hp210165), and the KAKENHI Grants (17K05433, 20K03981, JP19H05145, JP21H00117). The material presented here is based upon work supported in part by the U.S. Department of Energy, Office of Science, Office of Nuclear Physics, under Contract No. DE-AC02-06CH11357 (ANL).
- 1262 **Author Contributions** Y.K. designed and proposed the experiment, performed the offline analysis and the Monte Carlo simulations. Y.K., T.N., T.O., K.O., and N.A.O. drafted the manuscript. Y.K., T.N., N.L.A, H.F., L.A., T.A., H.B., K.B., C.C., D.C., H.C., N.C., A.C., F.D., A.D., Q.D., Z.D., C.A.D., Z.E., I.G., J.-M.G., J.G., A.G., M.N.H., A.H., C.R.H., M.H., A.H., Á.H., J.W.H., T.I., J.K., N.K.-N., S.K., S.K., K.K., T.K., D.K., S.K., I.K., V.L., S.L., F.M.M., S.M., J.M., K.M., T.M., M.N., K.N., N.N., T.N., A.O., F.O.S., N.A.O., H.O., T.O., V.P., S.P., A.R., D.R., A.T.S., T.S., M.S., H.S., Y.S., H.S., F.S., P.S., M.S., Y.S., H.S., D.S., O.S., L.S., S.T., M.T., M.T., H.T., Y.T., T.T., J.T., J.T., T.U., H.W., Z.Y., M.Y., and K.Y. took part in the setting up of the experiment and/or monitored the data accumulation and/or maintained the operation of experiment

1276 and detectors. T.O., N.S., N.T., Y.U. and S.Y. performed the
1277 EEdf3 calculations. K.O. performed the DWIA calculations.
1278 A.E., C.F., G.H., W.G.J., T.P., Z.H.S., and I.V. performed the
1279 coupled-cluster calculations and their statistical analysis and
1280 wrote the associated sections of the manuscript.

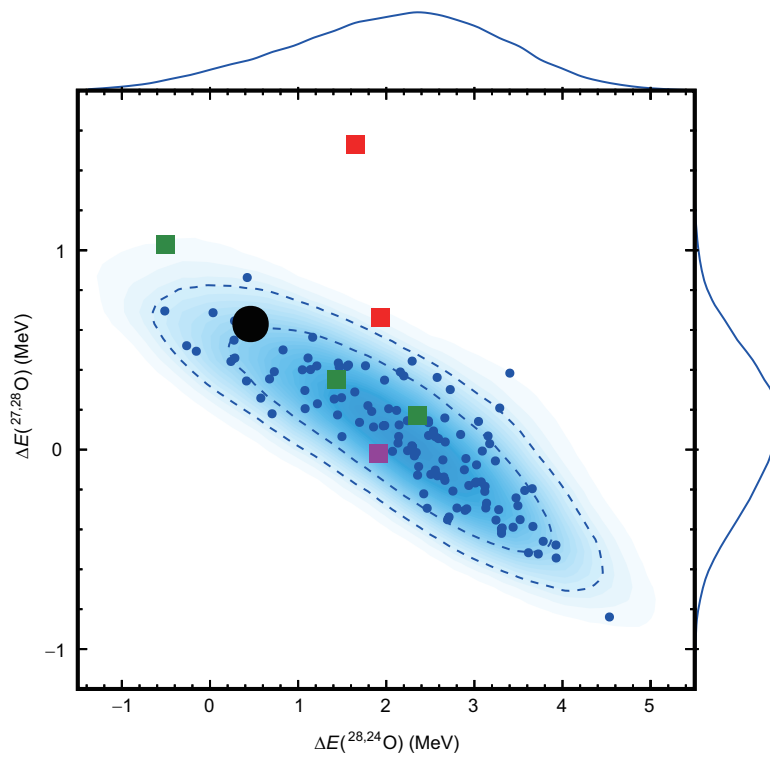
1281 **Competing Interests** The authors declare no competing in-
1282 terests.



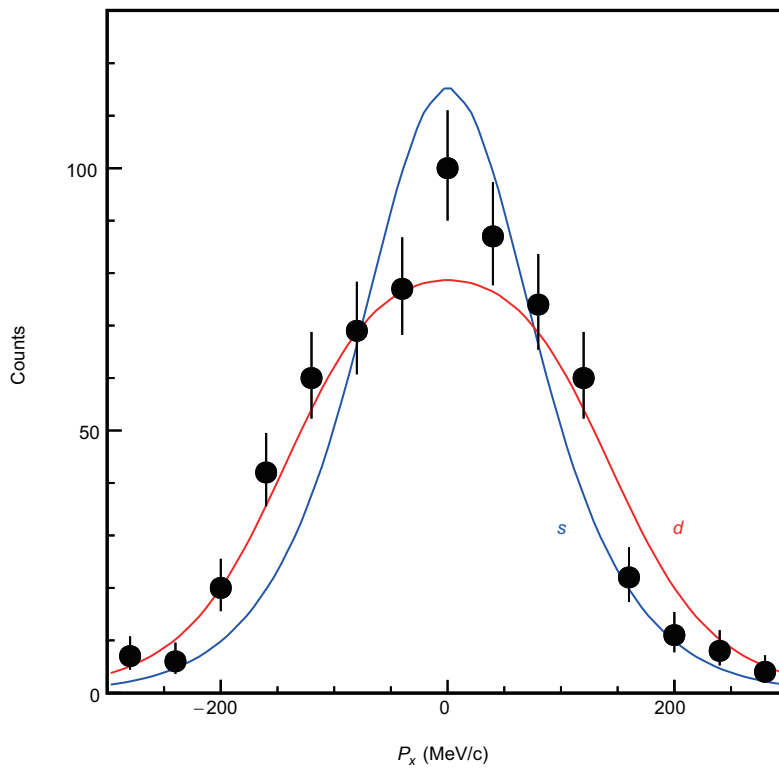
Extended Data Fig. 1 | Schematic view of the experimental setup. The insets show the overall efficiency as a function of decay energy for detecting $^{24}\text{O} + 3$ and $^{24}\text{O} + 4$ neutrons.



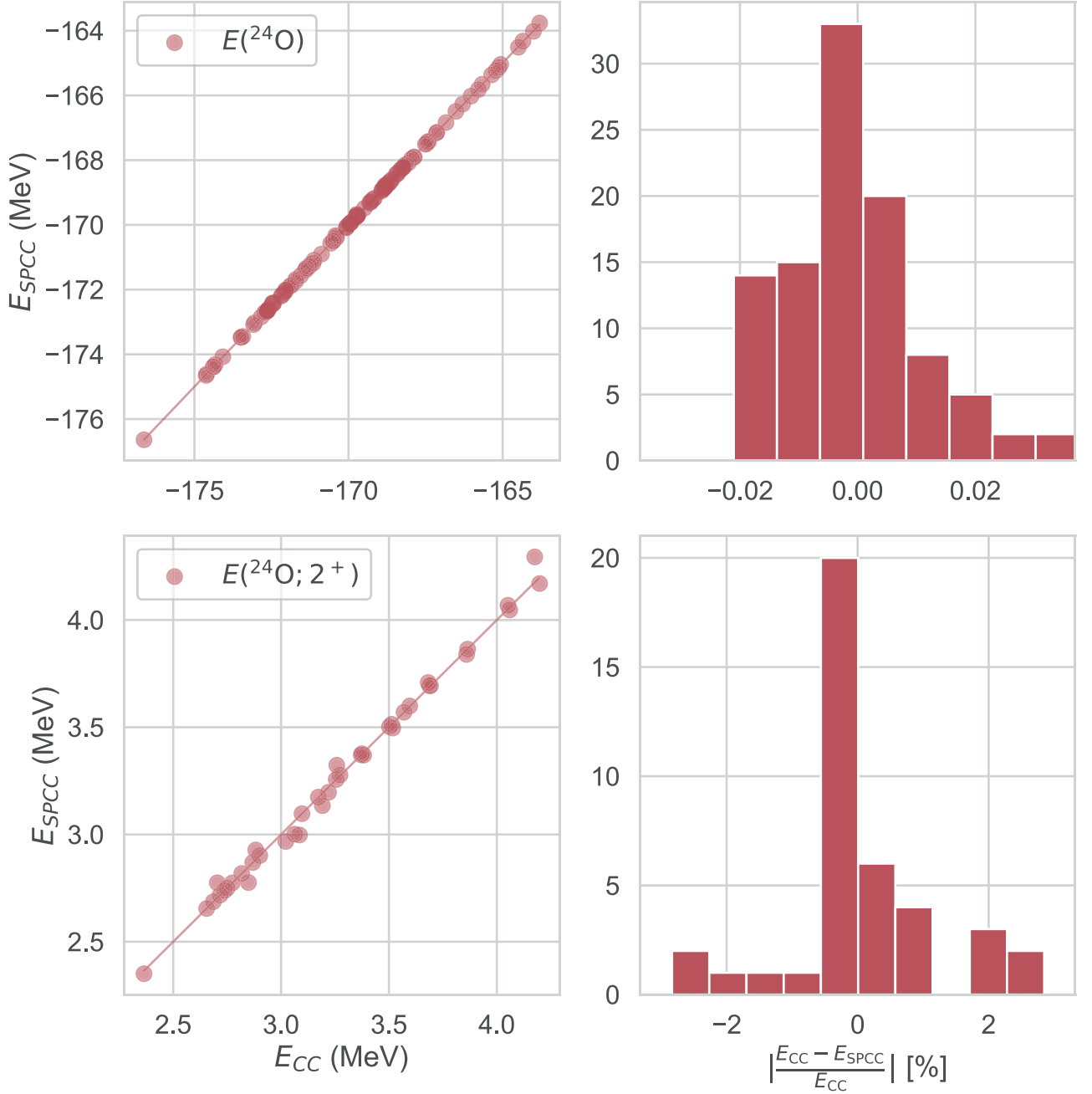
Extended Data Fig. 2 | Partial decay energy spectra. **a**, The filled grey histogram is the three-body decay energy E_{012} gated on the total decay energy $E_{01234} < 1$ MeV for the $^{24}\text{O}+4n$ coincidence events. The red and blue histograms are the results of simulations of sequential decay via the ^{26}O ground state (A and B in Fig. 2e) and five-body phase space decay, respectively. **b**, Same as a, but for the three-body decay energy E_{034} . **c**, The filled grey histogram is the partial decay energy spectrum E_{012} gated by $1.0 < E_{0123} < 1.2$ MeV for the $^{24}\text{O}+3n$ coincidence events. The red and blue dashed histograms are the results of simulations assuming ^{27}O sequential (B and C in Fig. 2e) and four-body phase space decay, respectively. The green hatched histogram represents the contribution from the decay of ^{28}O . The red (blue) solid histogram is the sum of the contributions from ^{28}O and ^{27}O for sequential (phase space) decay. **d**, Same as c, but for the two-body decay energy E_{03} . **e**, Decay energy spectrum of $^{24}\text{O}+2n$ events from the ^{29}Ne beam data. The grey histogram represents events with $E_{01} < 0.08$ MeV. The red histogram shows the results of the simulation for the decay of the ^{27}O resonance. The excess observed near zero decay energy is interpreted as arising from direct population of the ^{26}O ground state from ^{29}Ne . **f**, Decay energy spectrum of $^{24}\text{O}+2n$ events from the ^{29}F beam. The grey histogram represents events with $E_{01} < 0.08$ MeV. The red histogram shows the best fit in the region of the peak arising from the decay of the ^{27}O resonance (dashed histogram) and an exponential distribution (dotted curve) arising from all other contributions which come primarily from the decay of ^{28}O .



Extended Data Fig. 3 | Probability distribution of the calculated energy differences. Survived non-implausible calculations are shown by blue dots as functions of energy differences $\Delta E(^{28,24}\text{O})$ and $\Delta E(^{27,28}\text{O})$. The black circle shows experiment. The dashed curves indicate 68% and 90% highest probability density regions. The top and right distributions are the 1-dimensional probability density distributions. The values given by the other theories are plotted as squares: green – USDB, GSM, and CSM, red –SDPF-M and EEdf3 and purple – VS-IMSRG.



Extended Data Fig. 4 | Transverse momentum distribution of the $^{24}\text{O}+3n$ system in the rest frame of the ^{29}F beam. Events corresponding to the population of the ^{28}O ground state ($E_{012} < 0.08$ MeV and $E_{0123} < 0.8$ MeV) are shown by the data points. The blue and red solid lines represent the DWIA calculations, including the experimental effects for $s_{1/2}$ and $d_{5/2}$ proton knockout, respectively, whereby the distributions have been scaled to best fit experiment.

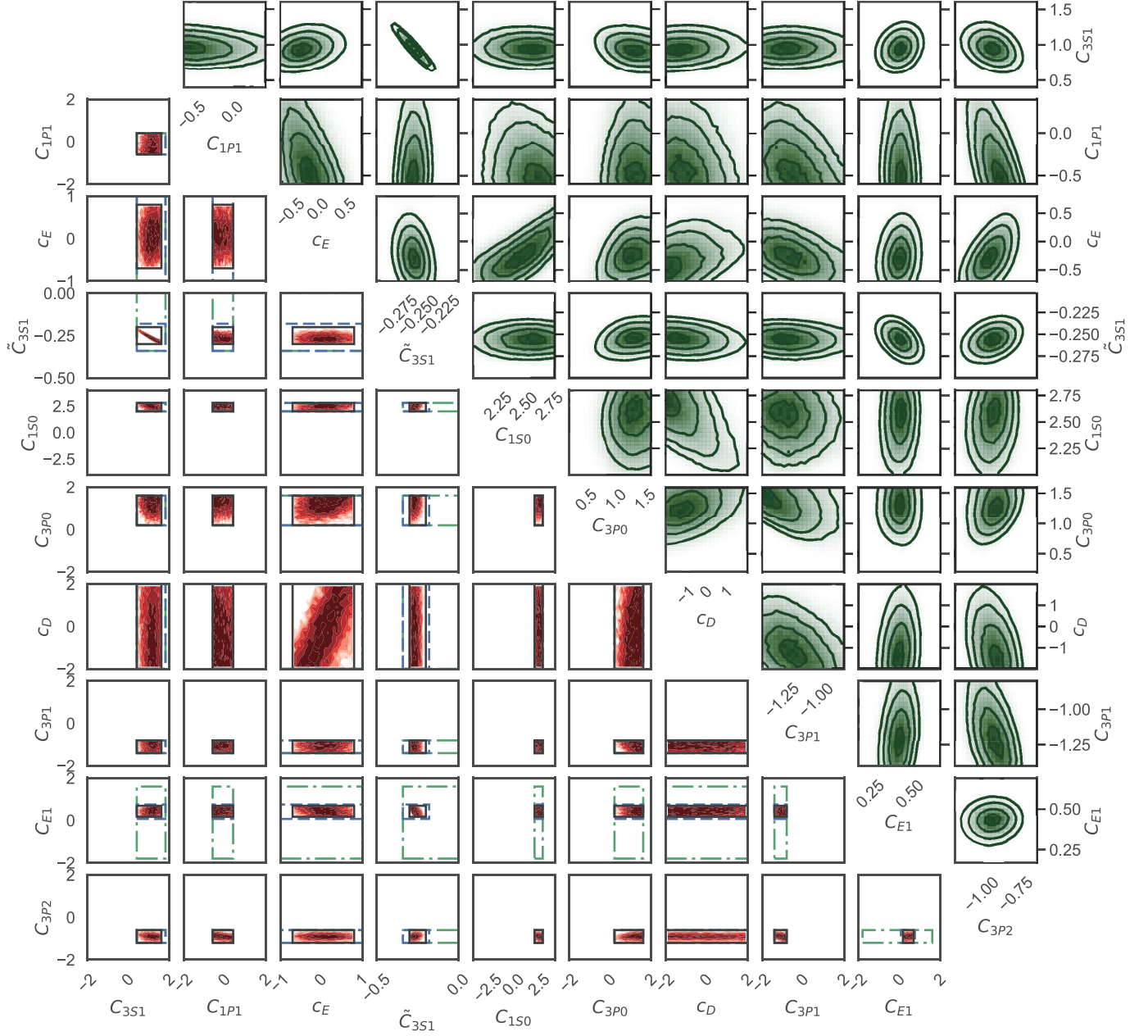


Extended Data Fig. 5 | Cross-validation of emulators. (Upper left panel) Total energies of ^{24}O computed with the coupled-cluster method in the CCSDT-3 approximation versus the SP-CC emulator for a validation set of 100 parameter samples. (Upper right panel) Distribution of residuals in percent. (Lower left panel) 2^+ excitation energies of ^{24}O computed with the coupled-cluster method in the EOM-CCSDT-3 approximation versus the SP-CC emulator for a validation set of 40 parameter samples. (Lower right panel) Distribution of residuals in percent.

Target	z	ϵ_{exp}	ϵ_{model}	ϵ_{method}	$\epsilon_{\text{emulator}}$
$E(^2\text{H})$	-2.2298	0.0	0.05	0.0005	0.001%
$r_p^2(^2\text{H})$	3.9030	0.0	0.02	0.0005	0.001%
$Q(^2\text{H})$	0.27	0.01	0.003	0.0005	0.001%
$E(^3\text{H})$	-8.4818	0.0	0.17	0.0005	0.005%
$E(^4\text{He})$	-28.2956	0.0	0.55	0.0005	0.005%
$r_p^2(^4\text{He})$	2.1176	0.0	0.045	0.0005	0.05%
$E(^{16}\text{O})$	127.62	0.0	0.75	1.5	0.5%
$r_p^2(^{16}\text{O})$	6.660	0.0	0.16	0.05	1%
$\Delta E(^{22,16}\text{O})$	-34.41	0.0	0.4	0.5	1%
$\Delta E(^{24,22}\text{O})$	-6.35	0.0	0.4	0.5	4%
$E_{2^+}(^{24}\text{O})$	4.79	0.0	0.5	0.25	2%
$\Delta E(^{25,24}\text{O})$	0.77	0.02	0.4	0.25	—

Extended Data Table 1 | Error assignments used in the statistical analysis. Energies in (MeV), squared point-proton radii in (fm^2) and the deuteron quadrupole moment in ($e^2\text{fm}^2$). $\Delta E(^{25,24}\text{O})$ is used in the Bayesian update step and the experimental target is from Hoffman et al.²⁴. This observable is computed in particle-attached coupled-cluster theory⁸⁴ and does not involve an emulator.

Target	z	ϵ_{exp}	ϵ_{model}	ϵ_{method}	$\epsilon_{\text{emulator}}$
$E(^2\text{H})$	-2.2298	0.0	0.05	0.0005	0.001%
$r_p^2(^2\text{H})$	3.9030	0.0	0.02	0.0005	0.001%
$Q(^2\text{H})$	0.27	0.01	0.003	0.0005	0.001%
$E(^3\text{H})$	-8.4818	0.0	0.17	0.0005	0.005%
$E(^4\text{He})$	-28.2956	0.0	0.55	0.0005	0.005%
$r_p^2(^4\text{He})$	2.1176	0.0	0.045	0.0005	0.05%
$E(^{16}\text{O})$	127.62	0.0	0.75	1.5	0.5%
$r_p^2(^{16}\text{O})$	6.660	0.0	0.16	0.05	1%
$\Delta E(^{22,16}\text{O})$	-34.41	0.0	0.4	0.5	1%
$\Delta E(^{24,22}\text{O})$	-6.35	0.0	0.4	0.5	4%
$E_{2^+}(^{24}\text{O})$	4.79	0.0	0.5	0.25	2%
$\Delta E(^{25,24}\text{O})$	0.77	0.02	0.4	0.25	—



Extended Data Fig. 6 | History-matching waves and Bayesian posterior sampling. (Lower left triangle) The panel limits correspond to the input volume of wave 1. The domain is iteratively reduced and the input volumes of wave 2, 3, 4 are indicated by green/dash-dotted, blue/dashed, black/solid rectangles. The optical depths of non-implausible samples in the final wave are shown in red with darker regions corresponding to a denser distribution of non-implausible samples. (Upper right triangle) Parameter posterior pdf from MCMC sampling with the non-implausible samples of the history-matching analysis as starting points. We use an uncorrelated, multivariate normal likelihood function and a uniform prior bounded by the first wave initial volume. Note that the relevant posterior regions are small in some directions, but larger in others such as c_D and c_E .

Wave	Target set (Z)	Number of active parameters	Number of input samples	NI samples fraction
1	np phase shifts	5–7	10^5 – 10^7	10^{-1} – 10^{-4}
2	$A = 2$	7	10^8	$2.3 \cdot 10^{-4}$
3	$A = 2$ –4	13	10^8	$3.4 \cdot 10^{-5}$
4	$A = 2$ –4, 16–24	17	$5 \cdot 10^8$	$1.3 \cdot 10^{-6}$

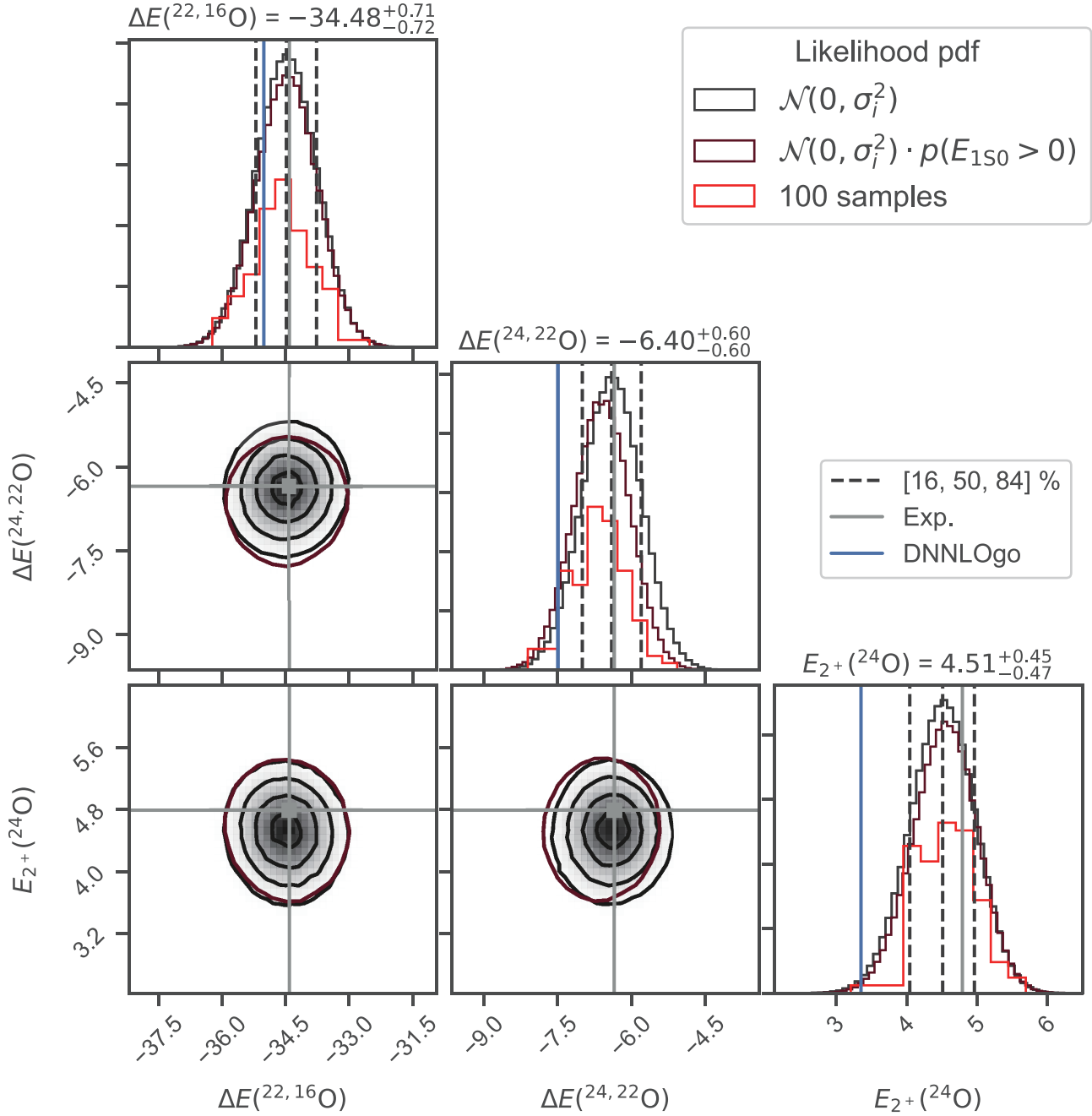
Extended Data Table 2 | Definitions of history-matching waves used in this work. The np phase shifts correspond to six targets ($T_{\text{lab}} = 1, 5, 25, 50, 100, 200$ MeV) for $^1S_0, ^3S_1, ^1P_1, ^3P_0, ^3P_1, ^3P_2$ partial waves. The $A = 2$ observables are $E(^2\text{H}), r_p(^2\text{H}), Q(^2\text{H})$, while $A = 3, 4$ are $E(^3\text{H}), E(^4\text{He}), r_p(^4\text{He})$. Finally, $A = 16 - 24$ correspond to $E(^{16}\text{O}), r_p(^{16}\text{O})$, the binding-energy differences $\Delta E(^{24,22}\text{O}), \Delta E(^{22,16}\text{O})$ and $E_{2^+}(^{24}\text{O})$.

Wave	Target set (Z)	Number of active parameters	Number of input samples	NI samples fraction
1	np phase shifts	5–7	10^5 – 10^7	10^{-1} – 10^{-4}
2	$A = 2$	7	10^8	$2.3 \cdot 10^{-4}$
3	$A = 2$ –4	13	10^8	$3.4 \cdot 10^{-5}$
4	$A = 2$ –4, 16–24	17	$5 \cdot 10^8$	$1.3 \cdot 10^{-6}$

Parameter	median	68% credible region
\tilde{C}_{1S0pp}	-0.343	[-0.360, -0.327]
\tilde{C}_{1S0np}	-0.339	[-0.352, -0.328]
\tilde{C}_{1S0nn}	-0.337	[-0.349, -0.327]
\tilde{C}_{3S1}	-0.258	[-0.272, -0.245]
C_{1S0}	2.502	[2.377, 2.785]
C_{3P0}	1.343	[1.217, 1.600]
C_{1P1}	-0.273	[-0.600, -0.115]
C_{3P1}	-1.074	[-1.199, -0.834]
C_{3S1}	0.982	[0.803, 1.160]
C_{E1}	0.437	[0.358, 0.512]
C_{3P2}	-0.920	[-1.032, -0.809]
c_1	-0.740	[-0.760, -0.721]
c_2	-0.494	[-0.645, -0.347]
c_3	-0.645	[-0.841, -0.456]
c_4	0.958	[0.861, 1.056]
c_D	-0.460	[-1.955, 0.175]
c_E	-0.107	[-0.471, 0.196]

Extended Data Table 3 | Medians and 68% credible regions (highest-density intervals) from the Bayesian posterior pdf of χ EFT model parameters obtained with MCMC sampling as described in the text.

Parameter	median	68% credible region
\tilde{C}_{1S0pp}	-0.343	[-0.360, -0.327]
\tilde{C}_{1S0np}	-0.339	[-0.352, -0.328]
\tilde{C}_{1S0nn}	-0.337	[-0.349, -0.327]
\tilde{C}_{3S1}	-0.258	[-0.272, -0.245]
C_{1S0}	2.502	[2.377, 2.785]
C_{3P0}	1.343	[1.217, 1.600]
C_{1P1}	-0.273	[-0.600, -0.115]
C_{3P1}	-1.074	[-1.199, -0.834]
C_{3S1}	0.982	[0.803, 1.160]
C_{E1}	0.437	[0.358, 0.512]
C_{3P2}	-0.920	[-1.032, -0.809]
c_1	-0.740	[-0.760, -0.721]
c_2	-0.494	[-0.645, -0.347]
c_3	-0.645	[-0.841, -0.456]
c_4	0.958	[0.861, 1.056]
c_D	-0.460	[-1.955, 0.175]
c_E	-0.107	[-0.471, 0.196]



Extended Data Fig. 7 | Posterior predictive distributions for $^{16,22,24}\text{O}$. MCMC samples of the posterior predictive distribution for selected oxygen observables. The black (maroon) histogram shows results obtained with an uncorrelated, Gaussian likelihood (including a discrete probability $p(E_{np,1S0} > 0|\theta) = 1$). The red histogram illustrates a low-statistics sample. The 68% credible regions and the medians are indicated by dashed lines on the diagonal, while the solid, vertical grey (blue) lines show the experimental target (prediction with the $\Delta\text{NNLO}_{\text{GO}}$ (394) interaction).